AIAA Journal
Vol. 60, No. 6, June 2022

Wall Pressure Spectra and Convection: Two-Dimensional Analysis Under Mean Pressure Gradients

Simon L. Prigent,* Édouard Salze,† and Christophe Bailly‡
Laboratoire de Mécanique des Fluides et d'Acoustique, UMR5509, 69130, Ecully, France

https://doi.org/10.2514/1.J060980

Wall pressure fluctuations beneath turbulent boundary layers subjected to a pressure gradient are studied in a subsonic channel flow, up to 76 $m \cdot s^{-1}$, where the test section's ceiling is adjusted to create the desired pressure gradients with the Clauser parameter ranging from −0.45 to 0.8. A rotating antenna of 63 nonuniformly distributed remote microphones enables a fine spatial resolution, down to 1 mm. The focus is put on the convective velocity, coherence scales, and two-dimensional wavenumber–frequency spectra. The convective velocity is increased by adverse pressure gradients, with values up to 14% higher than without gradient, which goes against the trend reported in previous studies. Both anisotropy and wall friction are increased by a favorable pressure gradient. In the subconvective region of the wavenumber–frequency spectra, classical models fail to match the data in terms of both levels and decay rates. Finally, the aspect ratio of these spectra's convective ridges is increased from adverse to zero, and then favorable pressure gradients. These results are discussed in light of the literature on coherent motion in boundary layers and how it is affected by pressure gradients. Mechanisms that could explain the observed pressure gradients' effects are finally proposed.

I. Introduction

OWING to the diverse nature of wall pressure fluctuations beneath a turbulent boundary layer, their understanding is of prime interest for the fields of aeroacoustics and vibro-acoustics. Applications can be found in the automotive and aeronautical industries [1,2], as well as in hydroacoustics studies [3,4] focused on marine technology, to cite only a few. In turn, intensive research has been carried into the field over the past seventy years or so, at first mostly in the absence of pressure gradient. Models for the spatial structure of the fluctuations have been proposed [5,6], along with some for the frequency spectra and are, to date, still commonly used in the industry despite known limitations to their validity. Indeed, measurements have been carried on that highlighted some of their limits, in particular at low and high frequencies [7] for the former. Some experimental [8] or numerical studies [9] had looked into turbulent boundary layers with pressure gradient, but available data has remained rather scarce for a long time, preventing a precise account of their effects. Reviews of this field of research were written at different stages [10,11] and offer a detailed account and discussion of the understanding of the matter at their time.

Since these reviews, the last two decades have seen a growing interest in the effects of pressure gradients. For instance, after Goody [12] proposed a new model for the frequency spectra, numerous studies have built onto it to extend its range of applicability, as discussed by Lee [13]. In particular, these models aim at describing the spectra for flows under adverse pressure gradients (apgs), since this corresponds to conditions found on the suction side of lifting airfoils, where diffraction of the pressure field at the trailing edge is a source of noise. However, these models tend to be tailored to specific flow conditions. As an illustration, measurements were conducted by Prigent et al. [14] on a wind tunnel mock-up of a private jet cockpit at velocities lower than cruise conditions. The reported spectra show limitations to the applicability of the discussed models for boundary layers developing on these industrial geometries. A better fundamental understanding of the pressure field, in terms of both spatial structure and frequency content, is thus needed, and research is still ongoing with experimental (e.g., [15]) or numerical studies (e.g., [16]). Despite the progress made thanks to various studies, previously discussed or omitted for brevity, some key questions are still open to debate, two of which are discussed hereafter and shall be addressed in the remainder of this work. Those are the effects of pressure gradients on the convective velocity and on the structure of the convective ridge of the wavenumber–frequency spectra. The latter is also linked to the determination of the subconvective levels of said spectra.

There are various ways of defining a convective velocity, in terms of phase velocity or group velocity for instance. The former requires the computation of space derivatives of the phase of the cross-spectra, which is often not available in experimental data due to a coarse spatial resolution. In turn, authors often report a different quantity directly computed from the phase of the cross-spectra at each frequency and separation, without spatial derivative, and which therefore depends on both frequency and spatial separation. On the other hand, the group velocity is usually computed by tracking the space-time path of the maximum of correlation; often referred to as broadband convective velocity, it depends on the spatial separation.

While there is a consensus that pressure gradients do affect the convective velocity, no clear quantitative description is reached. A model such as that by Smol'yakov [17] offers a good prediction for the frequency-dependent convective velocity in the case of zero-pressure-gradient (zpg) turbulent boundary layers. In the presence of pressure gradients, its coefficients must be adjusted, as pointed out by Salze et al. [18]. Catlett et al. [19] reported that two of these coefficients appeared to depend on the Clauser parameter and the third one on the boundary-layer aspect ratio.

Broadband convective velocity, or group velocity, has also been studied in the presence of pressure gradients. Schloemer [8] reported a reduction of about 14% from zpg to apg condition, at small spatial separation. However, only a few values of separation were available, and favorable pressure gradient (fpg) conditions could not be compared to either zpg or apg at a given normalized separation. Na and Moin [9] conducted direct numerical simulations that matched the data points of Schloemer [8] very well and were able to extent the comparison between cases, thanks to the spatial resolution. A strong reduction of the convective velocity was found from fpg to apg throughout the whole range of separations, from 18% at the highest separations to about 29% at the smallest. For a flat plate with pressure

Presented as Paper 2014-2909 at the 20th AIAA/CEAS Aeroacoustics Conference, Atlanta, GA, June 16–20, 2014; received 7 June 2021; revision received 15 December 2021; accepted for publication 30 December 2021; published online 31 March 2022.

*Post-Doctoral Fellow; also Univ Lyon, Ecole Centrale de Lyon, CNRS, Univ Claude Bernard Lyon 1, INSA Lyon.

†Research Engineer; also Univ Lyon, CNRS, Ecole Centrale de Lyon, Univ Claude Bernard Lyon 1, INSA Lyon.

‡Professor; also Univ Lyon, Ecole Centrale de Lyon, CNRS, Univ Claude Bernard Lyon 1, INSA Lyon. Senior Member AIAA.

gradients imposed by an overhanging airfoil, Hu and Herr [15] found a reduction of up to 18% from fpg to apg. The use of 12 probes indeed allowed for comparison of the different cases. Recently, Fritsch et al. [20] also used an overhanging airfoil, to study nonequilibrium flows with two subsequent and opposite pressure gradients. The authors reported lower convective velocities for apg conditions and higher ones for fpg, but close to no variation of the convective properties when normalized by outer variables. Interestingly, they [20] also reported that the flow history had a strong influence: a given pressure gradient leading to different results depending on whether it was the initial or secondary gradient. Burton [21] conducted measurements on the floor of a wind channel with fpg conditions imposed by an inclined ceiling and apg conditions by inclining the floor itself: a reduction of about 24% from fpg to apg was observed. Other studies focused on apg conditions, such as Catlett et al. [19] with a beveled trailing edge, and reported similar trends. However, a recent numerical study [16] found much less significant variations between fpg, apg, and zpg conditions, with variations of 5% at most and much smaller over a large range of separation.

Experimental data measured with a refined spatial resolution could therefore add knowledge to the effect of pressure gradients, both for the broadband convective velocity and for the frequency-dependent one. In particular, the spatial evolution of the phase of cross-spectra should enable the computation of the phase velocity.

The wavenumber–frequency formalism is a useful approach as it allows the differentiation of a range of scales at a given frequency, and it is therefore often used in academic applications [22]. Some experimental studies have looked into the one-dimensional wavenumber frequency spectrum (e.g., [14,23,24]), but data on two-dimensional wavenumber frequency spectra is very scarce. For instance, Panton and Robert [25] and Arguillat et al. [26] have looked at such spectra in laboratory conditions, with zero pressure gradient. Haxter and Spehr [28] analyzed flight test data to compute two-dimensional spectra, but the challenges of such an apparatus inherently lead to coarse results. In their numerical simulation, Cohen and Gloerfelt [16] observed a reduction of the convective ridge aspect ratio (for a given frequency) under apg conditions. A set of finely resolved spectra, with and without pressure gradient would be good to complement these observations from an experimental point of view.

Furthermore, it is now understood that although the convective ridge of the wavenumber spectrum clearly accounts for the majority of its energy, other less energetic components such as the subconvective range play a key role in vibroacoustics [28]. This is of particular interest in applications where the turbulent boundary layer developing on a fuselage induces a fluctuating pressure load that radiates noise inside a cabin, for passenger aircraft, train, or even cars. Despite several models having been developed for the wavenumber–frequency spectra, their predicted levels differ by up to 20 dB in the subconvective range as illustrated by Graham [1]. Little experimental data is available in that range due to the difficulty to measure pressure fluctuations across a wide range of scales and amplitudes without significant measurement errors.

Arrays of remote sensors are a robust way of measuring wall pressure fluctuations with a good spatial resolution and can be used when rear access to the studied surface is not an issue. Such arrays have gone a long way since initial two-point systems that were incrementally rotated to cover a wide range of separation [25]. Arrays of microphones distributed along a line on a rotating disk [18,26] offer the possibility to compute all cross-spectra at once for a given angular position. This has inspired others to look into rotating disks with spirals of microphones [29]. The antenna presented by Salze et al. [18] contains a nonuniformly distributed line of microphones that increases the resolution of the co-array in the separation space. These advances in microphones arrays, combined with deconvolution techniques [30], could help make a step forward. Furthermore, the ability to measure various quantities with the same setup and therefore the same boundary layer should also allow for a more global view of the topic.

A preliminary analysis of the data has been presented by Salze et al. [18]. The present study further analyses these experimental measurements to tackle the issues raised in the above discussion. After a description of the apparatus and flow conditions, Sec. III focuses on the frequency spectra, comparing them to previous data sets and looking at pressure gradients effects. Section IV then investigates the broadband and frequency-dependent convective velocities. Coherence and its length scales are detailed in Sec. V. Wavenumber–frequency spectra are studied in Sec. VI, and concluding remarks are finally drawn.

II. Experimental Conditions

Each experimental point considered in the present study is denoted by a configuration, namely zero-pressure gradient (zpg), adverse pressure gradient (apg) or favourable pressure gradient (fpg), and by a number associated with the local freestream velocity. For instance, apg38 refers to the apg case where the outer velocity at the measurement location is 38 $\mathrm{m.s^{-1}}$. Cases for which the freestream velocity is written in bold in Table 1 correspond to measurements with a rotation of the antenna: these are used for the computation of spatial quantities. The following sections detail the apparatus and relevant flow quantities.

A. Wind Tunnel

Measurements have been conducted in a bespoke test section mounted in the main anechoic subsonic wind tunnel of the Centre for Acoustic Research of the Fluid Mechanics and Acoustics Laboratory. The flow is generated by a 350 kW Neu centrifugal blower delivering a nominal mass flow rate of 15 $\mathrm{kg \cdot s^{-1}}$, and the fan is powered by an electronically controlled Tridge-Electric LAK 4280A motor. Air passes through a settling chamber including a honeycomb and several wire meshes designed to reduce freestream turbulence. Acoustic treatment on the wind tunnel walls and baffled silencers allows to reduce the inlet noise level and to prevent contamination of acoustic measurements performed in the anechoic chamber. This results in an inlet air flow at ambient temperature with a low background noise and low residual turbulence intensity, less than 1%. The reader is referred to Panton and Robert [25] and Arguillat et al. [26] for a more detailed description of the facility.

The test section itself is mounted in the anechoic chamber and connected to the inlet contraction as illustrated in Fig. 1. It is a closed channel purposely built for the study of boundary layers subjected to pressure gradients. The floor is a flat plate over which the boundary layer of interest develops and where instrumentation can be mounted. The boundary layer is not triggered and develops from the end of the contraction. The side walls of the second part of the channel ($L/2 < x_1 < L$) are made out of wire mesh and porous liner to reduce noise generated by the jet at the channel outlet. Finally, the two parts of the ceiling can be inclined to create a specific pressure gradient at the measurement location, indicated as $x_{1\mathrm{ref}} = 3h$ in Fig. 1, with h being the channel height at the inlet.

Three ceiling positions, with angles (α_1, α_2) for the two sections, have been investigated in this study. First, a zpg configuration has been set with the angles $(0.3°, 3.9°)$ to account for the slow boundary-layer growth. Second, a favorable or negative pressure gradient (fpg) corresponds to angles of $(-3.5°, 1.5°)$. Finally, an adverse or positive pressure gradient (apg) has been created with the angles set to $(4°, 4°)$.

The boundary-layer thickness δ has been found to remain small with respect to the channel height h in the test section, their ratio being about $\delta/h \simeq 0.08$. Independent boundary layers therefore develop on the floor and ceiling. Furthermore, mean pressure and velocity fields have been found homogeneous in the middle part of the channel, at least for $-0.6h \le x_2 \le 0.6h$, with details given below.

B. Mean Pressure Gradient

A specifically instrumented floor has been used for the characterization of the boundary layer, and replaced with the one fitted with the rotating antenna for the relevant measurements. The ceiling and therefore the pressure gradient were not modified during this process. This instrumented floor is fitted with static pressure probes distributed along three rows at $x_2 = 0$ and $x_2 = \pm 0.6h$ to measure the mean pressure distribution $\bar{p}$ along x_1. Mean static pressure data is recorded using a

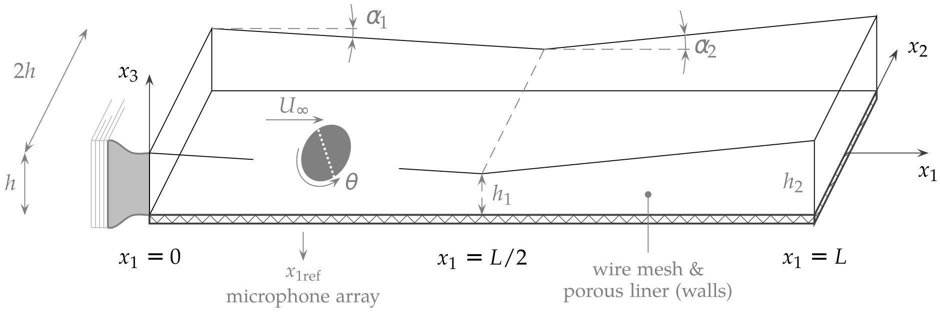

Fig. 1 Sketch of the test channel and notations. The height of the initial section is $h = 250$ mm, the length of the whole channel is $L = 16\,h$, and the location of the disk antenna is $x_{\mathrm{ref}} = 3\,h$. It should be noted that U_0 is the velocity at the channel inlet ($x_1 = 0$), and that U_∞ is the local freestream velocity of the boundary layer at the streamwise location of the measurement, that is, $x_{1\mathrm{ref}}$ for the rotating array.

Scanivalve system connected to a single Validyne dp15 pressure transducer.

The pressure coefficient is defined as $C_p = (\bar{p} - p_{\mathrm{amb}})/q_0$, where $q_0 = \rho_0 U_0^2/2$ is the dynamic pressure at the channel inlet $x_1 = 0$, and p_{amb} is the ambient pressure in the anechoic room. Without pressure gradient, it remains constant in the first part of the channel $0 \le x_1/h \le 8$, within a ± 0.008 variation. Its evolution along the channel center line $x_2 = 0$ is shown in Fig. 2 for the adverse (apg) and favourable (fpg) pressure gradient configurations at different velocities. In the measurement region (around $x_{1,\mathrm{ref}}$), transverse variation of the mean static pressure remains within 3% for apg cases and within 1% for fpg32. With low values of C_p in zpg conditions these variations are within 6% for zpg25 and 3% for zpg45 and zpg76.

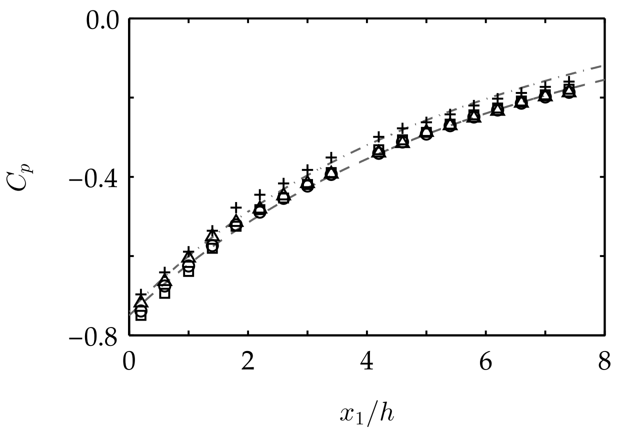

a)

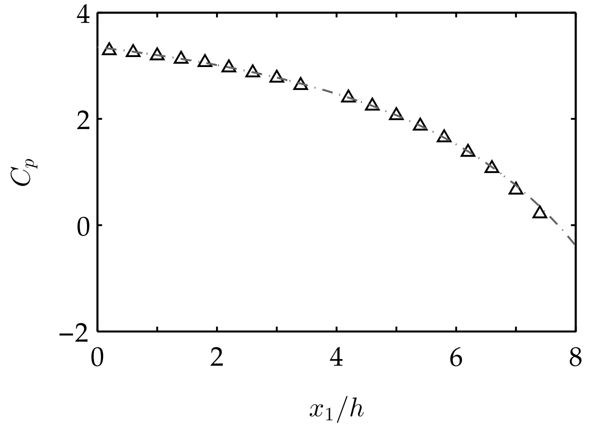

b)

Fig. 2 Longitudinal profile of the pressure coefficient C_p as a function of the dimensionless distance x_1/h. a) For Δ, apg19; °, apg38; ⋄, apg57; and +, apg74. b) For Δ, fpg32. The semi-empirical law (1) is also shown in gray lines.

Following the expression given by Dixit and Ramesh [31], the derivative of the pressure coefficient can be expressed as

$$\frac{dC_p}{dx_1} = -\frac{2L_0^2}{(L_0 - x_1)^3} \tag{1}$$

where L_0 is close to the length of the channel but must be adjusted because of installation effects. The values obtained from this semi-empirical law are also shown in Fig. 2. For the apg configuration the present data gives $L_0 = -14h$, except for apg74, for which $L_0 = -12.8h$, and $L_0 = 14.8h$ for the fpg configuration. The good match between the current data and this law means that, as expected for an inviscid flow, the streamwise derivative of the pressure coefficient does not depend on the velocity.

Using Eq. (1) and the previous values of L_0, the relative variation of (dC_p/dx_1) over the antenna's diameter is evaluated to about 18% for apg cases and 26% fpg. Following from Elsinga and Marusic [32], one can estimate the eddy turnover time as $\mathcal{T} \simeq 14 \times \delta/U_\infty$. Assuming, for the sake of the argument, that the convection velocity follows $U_c = 0.7 \times U_\infty$ and defining the convection time of an eddy over the antenna by the ratio between its diameter and said convection velocity, $\tau_c = D/U_c$, one has $\mathcal{T}/\tau_c = 10 \times \delta/D$. Using velocity data, which is detailed in the following section, this ratio is around unity for the studied cases. In that regard, one can consider the boundary layer to be out of equilibrium in terms of the effect of the pressure gradients, especially for the largest and long-lived eddies.

C. Boundary-Layer Velocity Profiles

Velocity profiles have been measured with a Dantec 55P01 hot-wire operating in constant voltage mode using a Streamline anemometer. Each measurement is conducted at a sampling frequency $f_s = 102.4$ kHz during 90 s. Spanwise variations of the outer mean velocity did not exceed 1% at $x \simeq x_{1,\mathrm{ref}}$. Downstream thickening of the boundary layer is particularly noticeable for apg flows, with variations over the antenna's diameter up to 37% for δ_1 and 36% for δ_2. The friction velocity was estimated by the Clauser method [33] using the mean velocity profiles, and was also checked against the output of a recent postprocessing method [34,35] based on a multi-parameter optimization scheme, accounting for errors in the estimation of the initial distance to the wall for instance. Variations did not exceed 2%. The profiles are fitted with the constants $\kappa = 0.41$ and $B = 4.9$ for the logarithmic law. Note that all the velocity profiles are located at $x_{1,\mathrm{ref}}$ in what follows. The obtained values are reported in Table 1. One can notice that with the velocities of interest, $\mathrm{Re}_{x_{\mathrm{ref}}} \simeq 5.3 \times 10^5$ is the lowest value obtained for the zpg cases. This indicates that the test section was designed to produce fully turbulent boundary layers, even more so since the latter ought to start developing upstream.

The velocity profiles in wall units for the three pressure gradients at various velocities are plotted in Fig. 3. The root-mean-square profiles exhibit the expected higher levels close to the wake region when the Reynolds number is increased. This effect is particularly visible for apg cases, which has been reported and discussed by Harun et al. [36]. The lack of a near-wall peak is due to the size of the hot-wire probe

Table 1 Boundary-layer parameters (velocities in $\mathrm{m \cdot s^{-1}}$ and lengths in m)

	U_∞	$\delta_1 \times 10^3$	H_{12}	u_τ	Re_{δ_1}	Re^+	Π	$K \times 10^7$	β	d_p^+
zpg	11	2.8	1.33	0.48	2.0×10^3	0.65×10^3	0.21	——	——	16
	25	**2.6**	**1.30**	**1.04**	4.3×10^3	1.3×10^3	**0.42**	——	——	**34**
	35	2.9	1.32	1.37	6.8×10^3	2.1×10^3	0.57	——	——	45
	45	**3.3**	**1.32**	**1.65**	9.9×10^3	2.7×10^3	**0.71**	——	——	**55**
	59	3.4	1.31	2.09	1.3×10^4	4.0×10^3	0.63	——	——	69
	76	**2.8**	**1.27**	**2.74**	1.4×10^4	4.8×10^3	**0.60**	——	——	**90**
apg	8.1	7.2	1.44	0.33	3.9×10^3	1.0×10^3	1.0	−2.9	0.79	10
	19	**5.9**	**1.44**	**0.68**	7.5×10^3	1.5×10^3	**1.2**	**−1.2**	0.73	**23**
	27	4.7	1.38	0.98	8.5×10^3	2.0×10^3	1.0	−0.88	0.56	33
	38	**4.6**	**1.31**	**1.35**	1.2×10^4	3.2×10^3	**0.81**	**−0.64**	0.59	**45**
	45	4.8	1.37	1.56	1.4×10^4	3.5×10^3	0.55	−0.53	0.63	52
	57	**4.3**	**1.34**	**1.95**	1.6×10^4	4.0×10^3	**0.83**	**−0.43**	0.60	**64**
	74	4.4	1.33	2.45	2.1×10^4	4.6×10^3	0.82	−0.34	0.68	80
fpg	10	2.0	1.29	0.51	1.4×10^3	0.86×10^3	−0.06	7.6	−0.45	17
	32	**2.0**	**1.26**	**1.35**	4.3×10^3	1.9×10^3	**0.10**	**2.5**	−0.59	**45**
	45	1.6	1.24	1.89	4.8×10^3	2.2×10^3	−0.02	1.8	−0.49	63

For velocities indicated in bold font, the antenna has been rotated.

being kept constant while varying the Reynolds number, which filters out the smallest fluctuations as highlighted in the study by Hutchins et al. [37]. The dimensionless sensing length of the wire, $l^+ = l \times u_\tau/\nu$, ranges from 40 to 226 for the zpg cases, 26 to 201 for the apg ones, and 42 to 158 for the fpg ones. Manufacturing a bespoke probe for each freestream velocity would have been beyond the scope

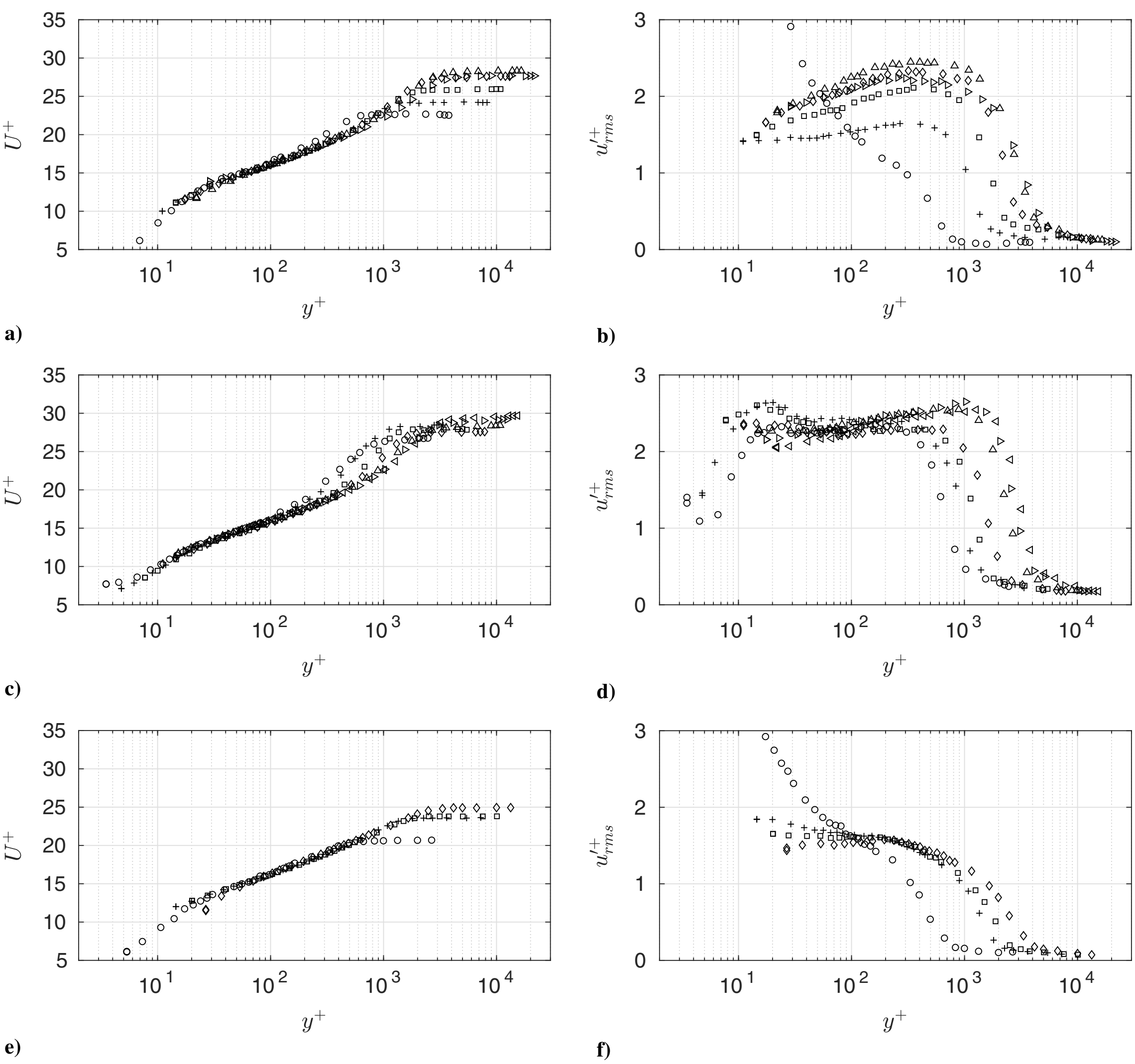

Fig. 3 Mean (a, c, e) and rms (b, d, f) profiles (at $x_{1,\mathrm{ref}}$) for zpg (a, b), apg (c, d), and fpg (e, f). Velocity order: ∘, +, □, ⋄, Δ, ▹, ◃, from lowest to highest in Table 1.

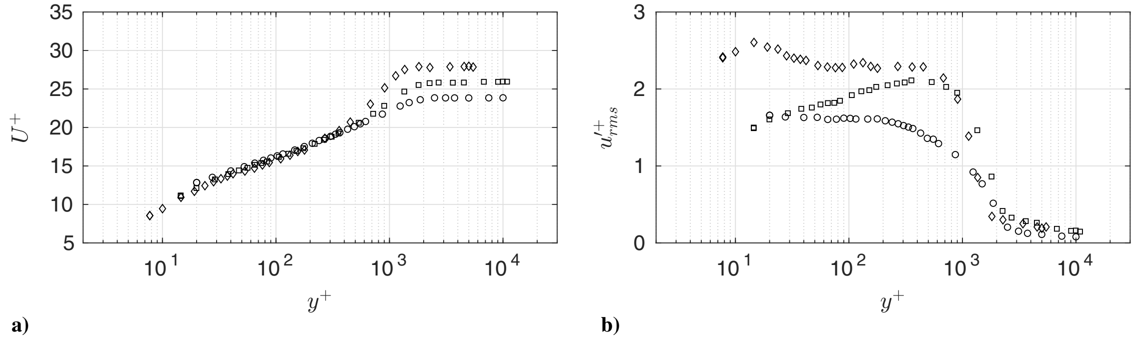

Fig. 4 Mean a) and rms b) profiles (at $x_{1,\mathrm{ref}}$) for apg (⋄), zpg (□), and fpg (°) at matching Reynolds number $\mathrm{Re}^+ \sim 2 \times 10^3$.

of the present study. The mean velocity profiles are well collapsed in the near-wall and logarithmic region for each pressure gradient. The zero-pressure-gradient profiles are in excellent agreement with previous studies such as that by Österlund [38] at matched Reynolds number, although the additional profiles are not shown here for readability.

Figure 4 shows the velocity profiles for the three pressure gradients at a matched Reynolds number. As expected [36], the mean profiles are similar in the near-wall and logarithmic regions but strongly differ close to the wake region. The apg case deviates from the logarithmic law at the smallest value of y^+ and has the highest wake value, contrary to the fpg case. The increase of the root-mean-square profiles at constant Reynolds from fpg to apg is clear in Fig. 4b. The increase in the wake region level is akin to what is observed for an increasing Reynolds number without pressure gradient.

D. Boundary-Layer Parameters

The mean velocity profiles are used to compute the boundary-layer parameters reported in Table 1: U_∞ is the local freestream velocity, δ_1 the boundary-layer displacement thickness, $H_{12} = \delta_1/\theta$ the shape factor with θ the momentum thickness, u_τ the friction velocity, $\mathrm{Re}_{\delta_1} = \delta_1 U_\infty/\nu$ the Reynolds number, and $\mathrm{Re}^+ = u_\tau \delta/\nu$ the Kármán number (where ν is the kinematic viscosity), and $\beta = (\delta_1/\tau_w) d\bar{p}/dx_1$ the Clauser parameter. The acceleration parameter K is also introduced $K = -(u_\tau^2/U_\infty^2)(\beta/\mathrm{Re}_{\delta_1})$ and Π is the wake parameter computed with the method of Esteban et al. [34] and Rodríguez-López et al. [35], using the exponential wake definition of Chauhan et al. [39].

The attention of the reader is brought to the small discrepancies, of a few tenths of millimeters, in the evolution of δ_1; however, the numerous repetitions of measurements to determine the transverse and downstream evolution of the boundary layer give confidence that this does not come from an ill-operated wind channel. Furthermore, both Reynolds number and friction velocity evolve in a consistent manner.

E. Pinhole Microphones

A pinhole microphone is used to measure the wall pressure spectra with a high-frequency response. To this purpose, an $1/8$ in Brüel and Kjær type 4138 microphone is fitted with a pinhole mask made of a perforated cap, whose diameter is $d_p = 0.5$ mm. This mounting's cutoff frequency is set by that of the cavity underneath the cap. Said cavity can be regarded as a Helmholtz resonator, but the theoretical determination of its resonance frequency would not be feasible. This resonance frequency is measured at $f_r \simeq 21$ kHz and the calibration procedure is detailed in Appendix A.

F. Rotating Antenna

The pressure antenna is composed of 63 identical remote microphone probes nonuniformly distributed along a line placed on a flush-mounted rotating disk. Each remote probe contains a $1/4$ in Brüel and Kjær type 4957 microphone, whose cutoff frequency is of about 15 kHz. The microphones are placed on the edge of steel tubes of variable diameter as illustrated in Fig. 5. The diameter of the last steel tube, flush fitted onto the surface of the rotating disk, is of

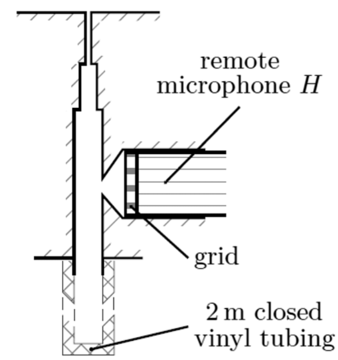

Fig. 5 Sketch of a remote microphone probe used to build the disk antenna (not to scale).

0.5 mm. A 2-m-long rear tube made of vinyl is used to dissipate pressure fluctuations and therefore avoid acoustic reflections. The antenna installed in the test section is shown in Fig. 6. This remote mounting reduces the sensing area of the probe and hence the averaging effect that damps the spectra at high frequencies and requires a correction, such as that developed by Corcos [40]. This correction is based on both the geometry of the sensor and the pressure correlation model, and the smaller the sensing area, the smaller the correction needed. A smaller sensing area also reduces the spacing between two neighboring probes, which allows for denser arrays of sensors.

For each measurement run, signal is recorded at 51.2 kHz during 90 s. Cross-spectra are computed for all combinations of sensors leading to a unique separation vector, at each angular position of the rotating disk. Details of the signal processing method used to compute the wavenumber–frequency spectra can be found in Prigent et al. [30]. The nonuniformity of the microphone distribution along the line increases the number of unique separations. While part of the data is processed with reference to the center microphone and therefore computed at 63 locations, space Fourier transformation is done under the assumption of homogeneity of the pressure field over the antenna and uses all 856 available positive unique separations. The antenna's disk is then rotated to 64 angular positions spanning $0 - \pi$, the other half of the full rotation being covered by symmetry of the antenna; see Appendix B for more details on the geometry.

III. Frequency Spectra

In order to compare the current results with previous studies, data was collected from publications at similar values of Re_θ by Schewe [41] with $\mathrm{Re}_\theta = 1.4 \times 10^3$, Farabee and Casarella [7] with $\mathrm{Re}_\theta = 3.4 \times 10^3$ and 4.4×10^3, Olivero-Bally et al. [42] with $\mathrm{Re}_\theta = 5.6 \times 10^3$, Gravante et al. [43] with $\mathrm{Re}_\theta = 5.0 \times 10^3$ and 7.1×10^3, Bull and Thomas [44] with $\mathrm{Re}_\theta = 7.0 \times 10^3$, Goody and Simpson [45] with $\mathrm{Re}_\theta = 7.3 \times 10^3$, and Blake [46] with $\mathrm{Re}_\theta = 10 \times 10^3$.

Spectra from zpg flows at various values of Re_θ, with and without the Corcos correction for the pinhole diameter, are displayed in Fig. 7. This correction takes into account the size and shape of the sensor as

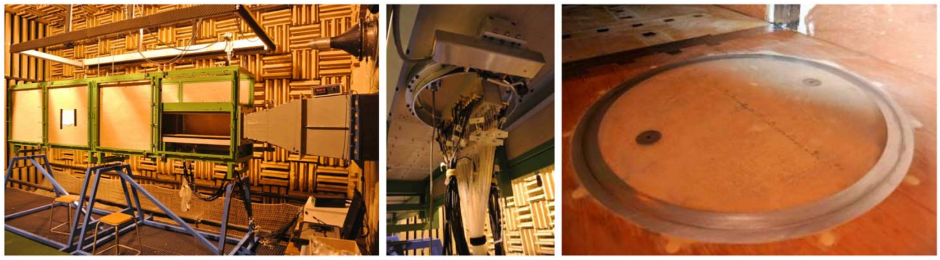

Fig. 6 Rotating antenna in the wind tunnel, from left to right: side view of the test section, bottom view of the disk with vinyl tubes and remote microphones, and top view of the disk.

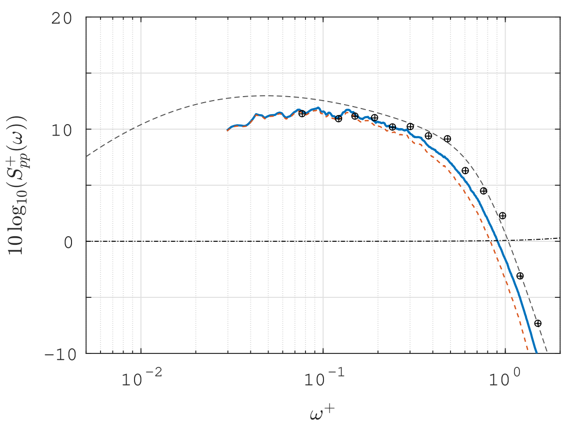

a) $Re_\theta \simeq 1.5 \times 10^3$

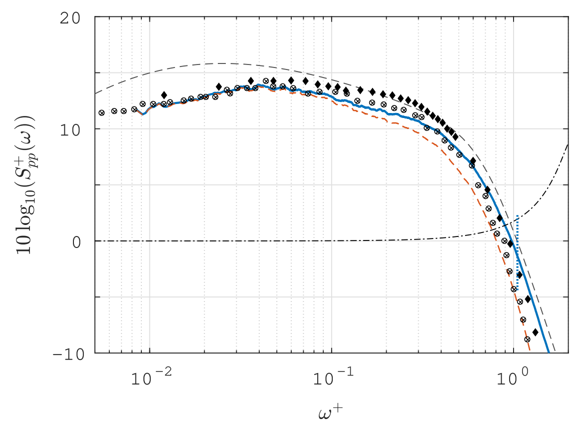

b) $Re_\theta \simeq 3.3 \times 10^3$

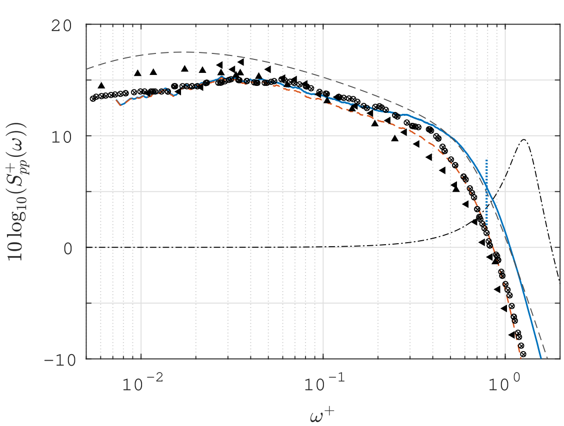

c) $Re_\theta \simeq 5.1 \times 10^3$

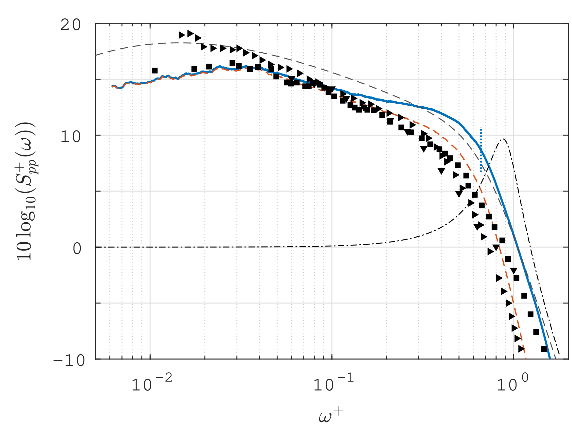

d) $Re_\theta \simeq 7.5 \times 10^3$

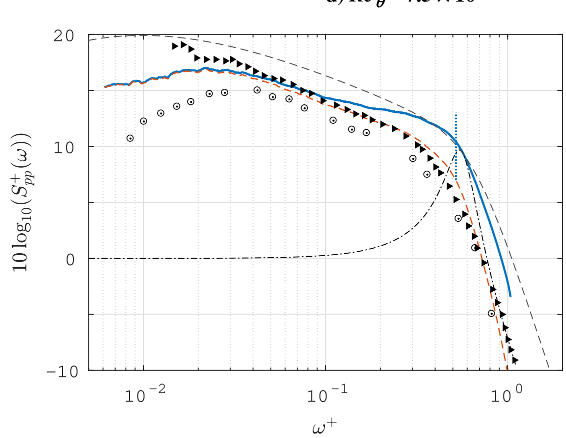

e) $Re_\theta \simeq 9.9 \times 10^3$

Fig. 7 Comparison of current data with previous studies at similar Re_θ: - - - zpg uncorrected, —— zpg corrected, - - - Goody model, ⊕ Schewe [56], ⊗ and ◆ Farabee and Casarella [23], ◀ and □ Gravante et al. [29], ▲ Olivero-Bally et al. [43], ▶ Goody and Simpson [25], ▼ Bull and Thomas [8], and ⊙ Blake [3]. Response of the microphone added for reference (dash-dotted). Vertical dotted lines indicate $\omega^+_{\max}$.

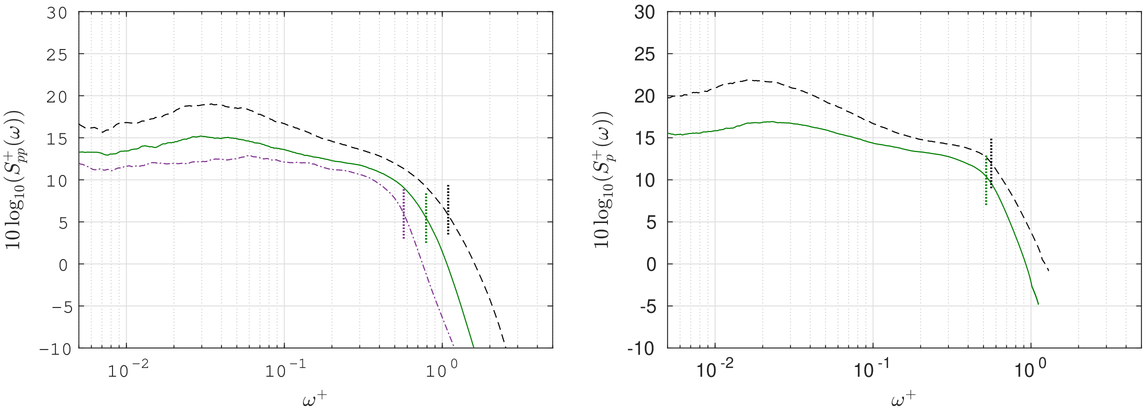

a) $Re^{+} \simeq 2\times10^{3}$ b) $Re^{+} \simeq 4\times10^{3}$

Fig. 8 Spectra from pinhole microphones for fpg (dash-dotted), zpg (solid), and apg (dashed). Vertical dotted lines indicate $\omega^{+}_{\max}$.

well as a model for the pressure fluctuations correlation. While more advanced models have been developed, the resulting correction for a moderate sensor size is not strongly affected, as illustrated by Prigent et al. [14]. Following the approach of Meyers et al. [47], the frequency above which this correction is significant is assumed inversely proportional to the nondimensional diameter of the pinhole d^{+}, and data from Gravante et al. [43] is used to compute it. The obtained value $\omega^{+}_{\max}$ is indicated by a vertical line in Figs. 7 and 8. The spectra are plotted against the previously mentioned experimental data and the Goody model [12], for reference. In addition to the acoustic treatment detailed in Sec. II.A, subtraction of the signal from two microphones was performed to remove the longitudinal acoustic mode of the channel; however this only affected the spectra at very low frequencies, out of the range displayed in this study. This subtraction is thus not done for the presented data.

At low Reynolds number, data from Schewe [41] is overall rather close to the current data, particularly in the midfrequency range. At $\mathrm{Re}_{\theta} \simeq 3.3\times10^{3}$, data from Farabee and Casarella [7] at $\mathrm{Re}_{\theta} = 3.4\times10^{3}$ is a close fit to the Corcos-corrected values up to $\omega^{+} \simeq 6\times10^{-1}$, after which it falls onto the uncorrected curve. Data from Farabee and Casarella [7] at $\mathrm{Re}_{\theta} = 4.4\times10^{3}$ depart further from the current case, in particular in the midfrequency range. At $\mathrm{Re}_{\theta} \simeq 5.1\times10^{3}$ again, data from Farabee and Casarella [7] is very close to the corrected curve and fall to the uncorrected one around $\omega^{+} \simeq 4\times10^{-1}$.

At $\mathrm{Re}_{\theta} \simeq 7.5\times10^{3}$, data from both Goody and Simpson [45] and Gravante et al. [43] match the current one around $\omega^{+} \simeq 10^{-1}$ and differ at higher values, whereas only that from Gravante et al. [43] has similar levels at low frequency. At the highest Reynolds number, $\mathrm{Re}_{\theta} \simeq 9.9\times10^{3}$, data sets from Goody and Simpson [45] (despite a lower Reynolds) and Blake [46] follow similar trends as the current ones for the midfrequency region (a.k.a. "overlap") and the high-frequency one (a.k.a. dissipation range), although not at the same levels. They also all differ for low frequencies, under $\omega^{+} \simeq 4\times10^{-2}$. It is worth noting the increase in difference introduced by the Corcos correction, which is particularly noticeable at the two highest Reynolds number.

A hump deforms the present spectra around $\omega^{+} \simeq 0.2$–0.8, between the overlap region and the dissipation range, and its effect increases with the value of Reynolds number. Its amplitude remains small, around 1–2 dB, but the shape is clearly visible. The response of the microphone is added to ensure that this is not due to the sensor itself. The hump is indeed visible for Reynolds numbers where the sensor's response is still flat in that frequency range. Meyers et al. [47] also reported this peculiar shape for smooth walls at Reynolds numbers higher than the present ones, spanning $\mathrm{Re}_{\theta} \simeq 36\times10^{3}$ to $\mathrm{Re}_{\theta} \simeq 69\times10^{3}$. Fritsch et al. [20] measured spectra for flows with various mean pressure gradients that also exhibited this shape. Meyers et al. [47] suggested that this inflection could be linked to the energy bottleneck observed in the dissipative range of velocity spectra for flows at high Taylor scale-based Reynolds number [48]. This bottleneck effect is very small and no evidence of its presence could be found in the velocity spectra determined from the hot-wire data acquired for the boundary-layer profiles.

Overall, the data collected from previous studies is rather scattered, even in the dissipative range where no good collapse is found. This goes to show the difficulty in comparing the data or semi-empirical models, with discrepancies in the measurement techniques and experimental conditions, and the challenge that measuring wall pressure represents. That being said, the present data is in fair agreement with the previously measured spectra across a large range of Reynolds number.

The spectra at matching Re^{+} for the different cases are plotted in Fig. 8. The reader is reminded that $S^{+}_{\mathrm{pp}} = S_{\mathrm{pp}} \times u_{\tau}^{2}/(\tau_{w}^{2}\nu)$ and $\omega^{+} = \omega \times \nu/u_{\tau}^{2}$. The curvature of the midfrequency range is visibly increased for the apg spectra. The levels are higher for apg than zpg and then fpg. In fact, Salze et al. [18] and Cohen and Gloerfelt [16] reported values of p'^{+}_{rms} as a function of Re^{+} from previous studies, and despite them being scattered one notices the trend for apg and fpg to exhibit higher and lower values than zpg, respectively.

A. Discussion

The effect of an fpg on the velocity structures within boundary layers has been the focus of several studies. For mildly accelerating boundary layers, Piomelli et al. [49] reported that the friction coefficient $C_f = \tau_w/q_{\infty}$ remains constant while U_{∞} increases, before an offset of relaminarization mechanism. This indicates that u_{τ} increases in the fpg flow. Bourassa and Thomas [50] reported that vortices are strongly elongated and that, by conservation of angular momentum, their rotational motions must increase. Although fewer of those vortices exist, potentially due to the straightening of the streak vorticity, their increased intensity may be the reason for the rise of friction velocity. Although the conditions of these studies are not those of the present one, an increase of friction velocity at given Reynolds numbers Re^{+} is indeed reported in Table 1. This is most likely a contributing factor to the reduction of p'_{rms} and correspondingly to the lowering of spectra measured for fpg cases.

IV. Convective Velocity

A classical definition of the frequency-dependent convective velocity from velocity fluctuations [51] is based on two-point measurements. This velocity is determined from the phase of the cross-spectrum of the two time series. Renard and Deck [52] pointed out that this first-order approximation could be refined. For Fourier modes, the local convective velocity could be defined as the phase velocity, which is computed as

$$U_c(f) = -\frac{2\pi f}{\left.\dfrac{\partial\Theta}{\partial r_1}\right|_{r_1=0}} \tag{2}$$

where $\Theta(r, f)$ is the phase of the cross-spectrum. Renard and Deck [52] discuss the fact that using power spectral density (PSD) estimates of the spectra leads to approximations in the derivation of the convective velocity and develop a more rigorous method to cope with this matter. However, this method requires the computation of space derivatives of the fluctuations prior to Fourier transformation, which is not available in the present study. In the following, the estimation of the frequency-dependent convective velocity is thus based on the evolution, in space, of the phase of the cross-spectra, making use of the refined antenna's spatial resolution. The reader should note that several studies (e.g., [7,8]) computed a convective velocity directly from the phase itself, and not its spatial evolution, giving a simultaneous dependence on both the frequency and the separation of the measurement probes in space. This formally differs from the current definition.

Another convective velocity can be defined from the analysis of the space-time correlation of the pressure fluctuations, noted $R_{\text{pp}}(r_1, 0, \tau)$ along the streamwise direction. The path of slowest correlation decay, either written $\xi_1(\tau)$ or $\tau_{\max}(r_1)$, corresponds to the trajectory of a reference frame in which the coherent structures decay at the smallest rate for the moving observer. Willmarth and Wooldridge [53] and Bull [54] have defined a convective velocity as that of this reference frame, yielding

$$U_c(r_1) = \left.\frac{d\xi_1}{d\tau}\right|_{\tau=\tau_{\max}(r_1)} \tag{3}$$

Bull [54] has also looked at the average value

$$\bar{U}_c(r_1) = \frac{r_1}{\tau_{\max}(r_1)} \tag{4}$$

often referred to as broadband convective velocity. Strictly speaking, the smallest value of separation r_1 should be used so that the quickly decaying structures are accounted for. Renard and Deck [52] showed that, in the limit of a vanishing separation, this correlation-based convection velocity is equivalent to one obtained through a weighted integration of the frequency-dependent one.

Both quantities are investigated in the following sections.

A. Frequency-Dependent Convective Velocity

Rather than computing the phase derivatives only on the smallest separation values, a linear fit is done that is a fair approximation over an extent of separation that varies with frequency. Figure 9a shows the phase of a cross-spectrum at a given frequency, as a function of the separation r with regard to a reference microphone taken at the center of the antenna. An automated routine iteratively excludes the outer data points until a linear fit of the remaining ones gives a low error resulting in $\epsilon^2 < 10^{-4}$ with the coefficient of determination given by $1 - \epsilon^2$. The obtained linear fit is also shown in Fig. 9a, and its slope is used for the computation of the convective velocity as per Eq. (2). The obtained value is then reported as a function of frequency in Figs. 9b–9d for the three pressure gradient cases and various outer velocities, smoothed with a simple 9-point running average. The Smol'yakov model [17] is also added, according to the relation

$$\frac{U_c}{U_\infty} = a\frac{\omega\delta_1/U_\infty}{1 + b(\omega\delta_1/U_\infty)^2} + c \tag{5}$$

where the constants $\{a, b, c\}$ are tailored to each pressure gradient case: the original values $\{1.6, 16, 0.6\}$ for zpg, the values $\{0.8, 3, 0.65\}$ for apg, and $\{1.4, 20, 0.7\}$ for fpg. Catlett et al. [19] reported that a and b appeared to depend on the Clauser parameter and c on the boundary-layer ratio, which could explain why the

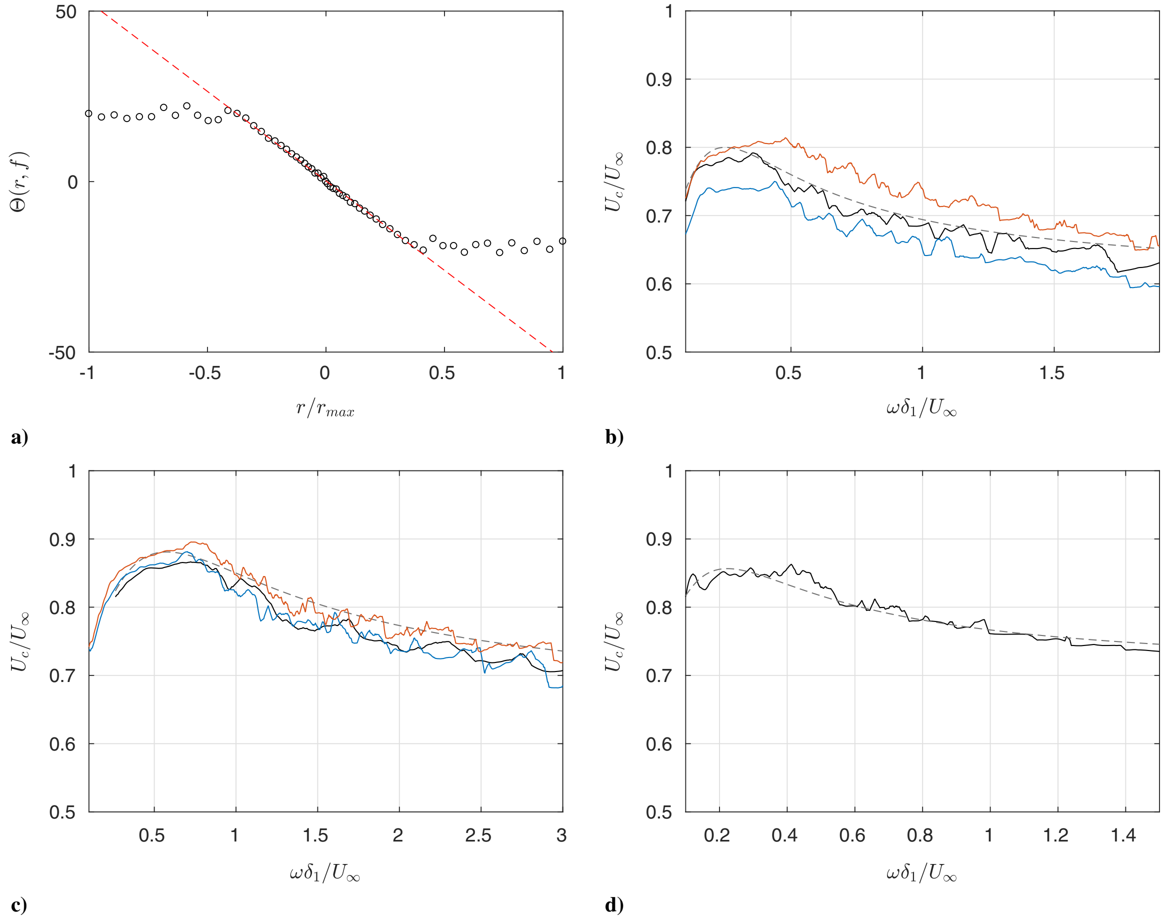

Fig. 9 Phase of the cross-spectra against separation, a) for zpg45 at 2 kHz. Frequency-dependent convective velocity (solid), and corresponding Smol'yakov models (dashed), for b) zpg25–zpg45–zpg76, c) apg19–apg38–apg57, and d) fpg32. Color order: black, blue, red.

present values of a and b differ more than those of c. The model is in good agreement with the data for the apg and fpg cases. For zpg boundary layers, the disparity is larger than for apg cases, with zpg76 displaying the highest convection velocity throughout the entire frequency range.

It is clear from Fig. 9 that the zpg cases exhibit the lowest convective velocity values of all three, with the highest for apg cases. The frequency corresponding to maximum convective velocity appears to be shifted to higher values from fpg to zpg and then apg. The latter indeed peaks at around $\omega\delta_1/U_\infty = 0.6$, whereas the former peaks at around $\omega\delta_1/U_\infty = 0.3$. A classical argument [8] to account for the variation of convective velocities between cases, with and without pressure gradient, is to look at their effect on the mean velocity profiles. One can associate each frequency with a length scale and assume that it should correspond to half the local height within the boundary layer. A pseudoconvective velocity is thus found for each frequency that directly reflects the possible modification of the profile. A refinement could be made iteratively, by taking the new velocity computed for a given frequency, and updating the corresponding length scale, thus leading to an updated velocity and so on until convergence is reached. This train of thoughts elegantly explains some discrepancies between cases but it must be taken with caution as the outcome of this approach is far from the measured convective velocity.

Should the dispersion relation $2\pi f = -U_c k_c$ be strictly verified, the convective velocity could also be computed via the convective wavenumber. Using the one-dimensional wavenumber–frequency spectrum, further discussed in Sec. VI, $k_c(f)$ can be estimated by tracking the maximum value of the convective ridge for each frequency. The convective wavenumber $k_c(f)$ is then smoothed prior to the computation of U_c. The convective velocity obtained with this convective wavenumber for zpg, along with the corresponding previously discussed values, is plotted in Fig. 10. While the peak values are fairly similar between the two methods, the peak itself appears to be narrower and shifted to lower frequencies for the wavenumber method. Overall, despite those discrepancies the curves remain similar.

B. Correlation-Based/Broadband Convective Velocity

In previous studies on the effect of pressure gradient [8,16], the broadband convection velocity has been reported as $\bar{U}_c(r_1)$ with the previous definition. For the sake of comparison, the same approach shall be followed. Note that the calibration of pressure signals is done in the frequency domain, using the transfer function of the remote microphone as explained in Appendix A. Hence the time series are not directly computed and correlation has instead been computed by inverse Fourier transforming the cross-spectra. This velocity is plotted in Fig. 11 for all gradients discussed in this study and normalized by the local freestream velocity U_∞.

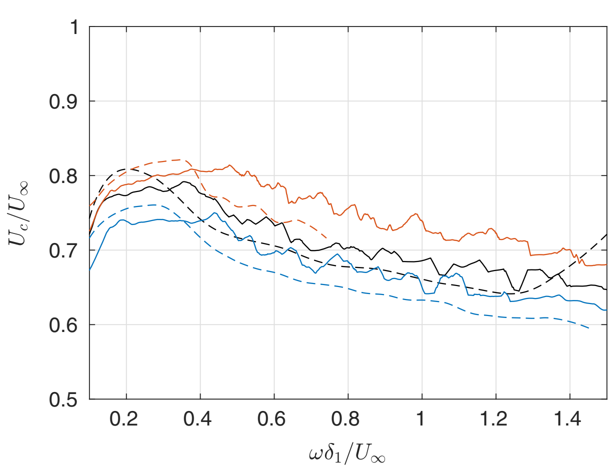

Fig. 10 Convective velocity for zpg25 (black), zpg45 (blue), and zpg76 (red): comparison between data obtained from cross-spectra phase (plain) and the convective ridge (dashed).

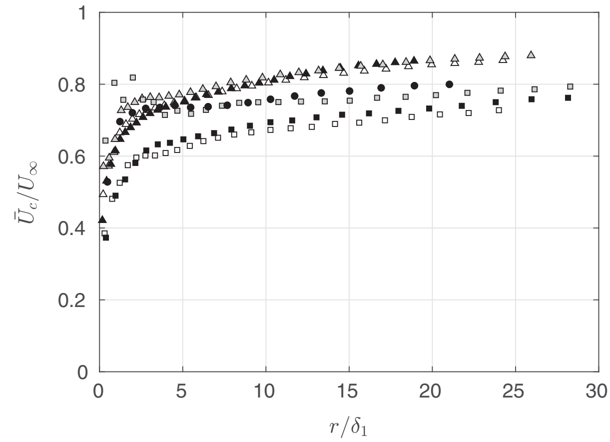

Fig. 11 Broadband convective velocity for apg19 (▲), apg38 (Δ), apg57 (Δ gray filling), zpg25 (□), zpg45 (□), zpg76 (□ gray filling), and fpg25 (•).

By looking at finite separations of increasing amplitude, one filters out the smallest scales that are short-lived. In turn, a large separation mainly reflects the larger scales that are classically attributed to a greater convective velocity, hence the increase observed in the curves. Therefore, should one decide to filter out the high-frequency data when computing $\bar{U}_c$, above the previously discussed $f^+_{\max}$, the result would marginally differ at small separations and not at larger ones. The apg cases display the highest values, with apg19 and apg38 being close within 1% except at the smallest value of separation; apg57 leads to higher values for $r/\delta_1 \leq 10$ but collapses well for larger separations. At $r/\delta_1 \simeq 5$, fpg32 is 3% smaller than apg19 and apg38 and this difference increases to 6% at $r/\delta_1 \simeq 20$. The zpg25 and zpg45 are within 5% of each other and are 13 and 14% smaller than apg38 at $r/\delta_1 \simeq 5$ and $r/\delta_1 \simeq 20$, respectively; zpg76, however, differs from the two previous ones and is closer to fpg32 at low separations. Final values, at large separations, are 0.87 for apg19 and apg57, and 0.86 for apg38; 0.73 for zpg25, 0.76 for zpg45, and 0.80 for zpg76; and 0.80 for fpg32. The same order is observed for the frequency-dependent convective velocity, so it is not surprising that it should be found in these broadband values. However, it is worth noting that the variations observed between pressure gradients are not in line with previous findings, discussed in the introduction, as apg conditions have been reported to reduce the convective velocity in several studies.

C. Discussions

The quantification of the pressure gradient's effects on the convective velocities greatly differs from study to study, which was presented in the introduction. Overall, apg flows had been reported to either reduce this velocity or have no significant influence, when compared to zpg flows. On the other hand, fpg flows had been reported to increase this convective velocity. Cohen and Gloerfelt [16] had illustrated this scatter, which highlighted how moderated the variations found in their results were. Despite the spread of reported values, the current results are at odds with previous findings.

As discussed before, Schloemer [8] proposed that the deformation of the mean profiles by pressure gradients could directly explain variations in the convective velocity, arguing that the latter could be estimated by the local mean velocity taken at a wall distance of half an eddy size. However, such a simplification of the eddy distribution in the boundary layer is a slippery slope. Indeed, Hutchins and Marusic [55] highlighted the presence of large-scale structures in the logarithmic region, whose length can be up to 20 times the boundary-layer thickness and which have a footprint on the near wall turbulence. Harun et al. [36] reported that an increased pressure gradient lead to more large-scale outer-region activity, although the superstructres are found to be shorter than in zpg flows. In turn, the apg flows were shown to have stronger near-wall footprint than for the zpg or fpg case. This goes along the observation of Monty et al. [56] that the increase in turbulent intensity across the boundary layer was in good part due to the energized large-scale log-region structures.

Near the wall, these large scale structures usually move faster than the local mean velocity [57–59]. This increased velocity near the wall, combined with the footprint of farther motions, could be a contributing factor to an increased convection velocity of wall pressure fluctuations beneath apg boundary layers. While this train of thoughts explains the trend observed in the present data, it cannot be the sole explanation and conflicting mechanisms ought to coexist, which would explain the discrepancies between reported studies.

V. Coherence and Its Length Scales

Discussing the different scales populating the boundary layer and the footprint they have in terms of wall pressure raises the question of the associated coherence. The coherence of pressure fluctuations beneath a turbulent boundary layer rapidly decays with separation, for a given frequency. This coherence, along the streamwise and spanwise directions, is reported in Fig. 12a for zpg45 at 2 kHz. Corcos [6] postulated that such decay should be exponential, depending on the ratio of separation to a coherence scale. The corresponding exponential fit is also shown in Fig. 12a, in the form $\exp(-r/L_i)$, i being either 1 or 2. Following this approach for each available frequency gives the evolution of the longitudinal (L_1) and transverse (L_2) coherence scales, as a function of frequency, reported in the other graphs of Fig. 12. At high frequencies, the antenna's finite resolution eventually prevents a satisfactory fit since not enough measurement points are available. For this reason, the computation of the coherence length scales is stopped at high frequencies when the r-square value of the fit drops below 0.9.

Three domains are observed; first, at low frequencies the longitudinal scales show little evolution and are within the range of $10\delta_1 - 20\delta_1$. The transverse ones decrease at the lowest frequency and reach a peak of $2\delta_1 - 3\delta_1$. In fact, in Smol'yakov model, which takes into account viscosity and finite thickness of the boundary layer to build onto the Corcos model, these scales are found to tend to $32\delta_1$ for the longitudinal one and $5\delta_1$ for the transverse one, when the frequency tends to zero. Such values are slightly higher than the present data, but show a satisfactory agreement nonetheless.

In the midfrequency range, they do not exactly decay at the ω^{-1} rate found in the Corcos model. The expectation for this decay rate is rooted in the assumption that the coherence should decay exponentially and depend only on the single dimensionless parameter $\omega r/U_c$. Should this be true, curves of coherence as a function of separation r obtained at different frequencies ω_0 would collapse. Although this is not shown for brevity, no satisfactory collapse is found in the present data. The decay rate is visible in Fig. 12, where both ω^{-1} and $\omega^{-1.5}$ are plotted for reference. For $\omega\delta_1/U_\infty \sim 0.2 - 0.7$ the decay is rather close to a ω^{-1} rate for the longitudinal length scale, but slightly steepens afterward. The decay rate is slower for the transverse scale.

At high frequencies, the curves deviate from the power law and tend toward a plateau. When expressed in terms of internal scales, this plateau is of the order of $1.0 \times 10^2 \nu/u_\tau$ for zpg25, $1.7 \times 10^2 \nu/u_\tau$ for zpg45, and $2.5 \times 10^2 \nu/u_\tau$ for zpg76 for the longitudinal and $20\,\nu/u_\tau$, $25\,\nu/u_\tau$, and $55\,\nu/u_\tau$, respectively, for the transverse scales. This lower bound is also taken into account in the Smol'yakov model, with a plateau at about $100\nu/u_\tau$, to account for viscosity effects.

Figure 12d shows the ratio of both scales for the three cases, which lies between 0.1 and 0.4. The attention of the reader is drawn on the fact that contrary to the velocity coherence scales where a vector is decorrelated along its transverse direction, L_2 corresponds to the decorrelation of a scalar that is moreover a nonlocal variable. The ratio L_2/L_1 gives an indication of the anisotropy of the pressure field, as it would be equal to 1 in an isotropic case. A strong anisotropy is

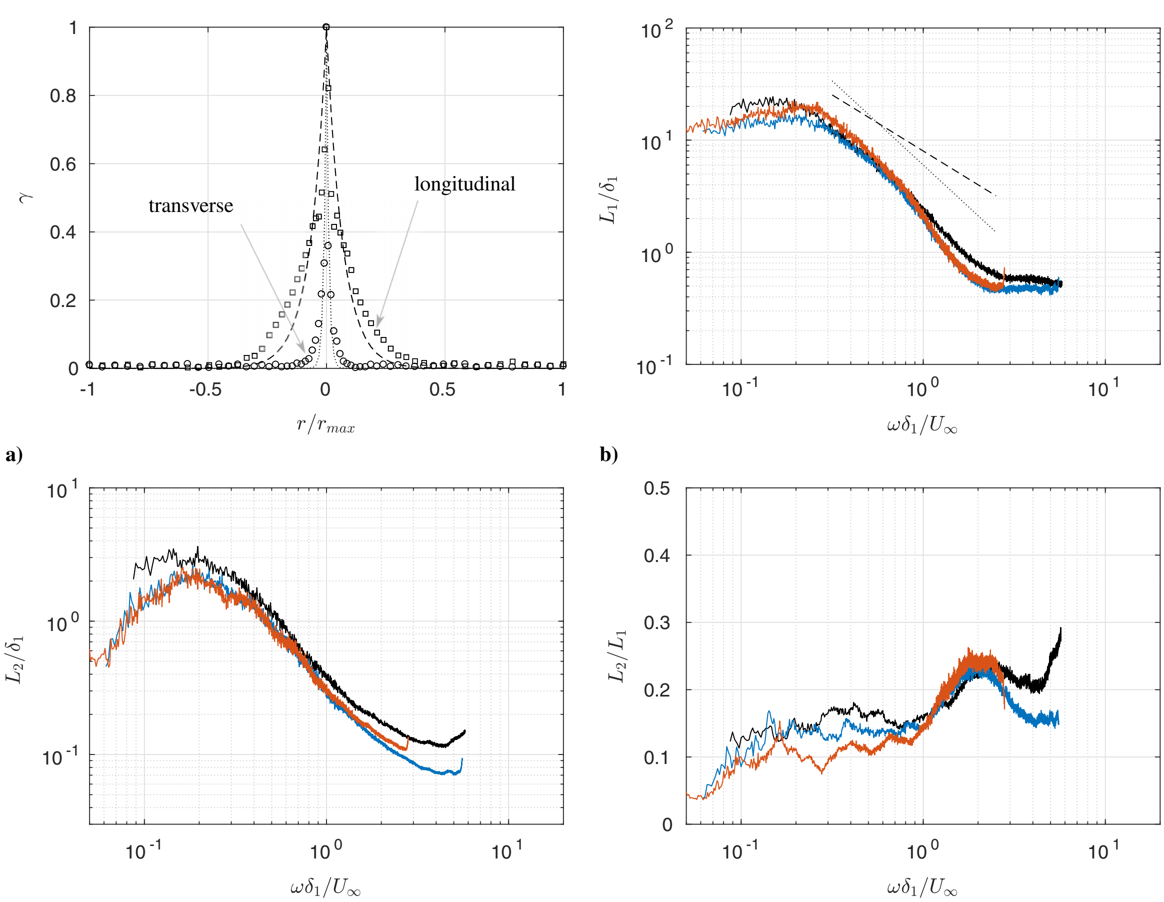

Fig. 12 a) Longitudinal and transverse coherence and their exponential fit for zpg45 at 2 kHz. b) Longitudinal and c) transverse length scales, and d) their ratio for zpg25 (black), zpg45 (blue), and zpg76 (red) cases. −1 (dashed) and −1.5 (dash-dotted) power laws for reference in b).

observed at low frequencies and it decreases with frequency. One could argue that this is due to larger vortices or structures, roughly speaking corresponding to lower frequencies, being elongated in the turbulent boundary layer.

The coherence scales for the apg cases, displayed in Fig. 13, exhibit the same three regions as the zpg cases. The upper bounds are similar to those previously discussed and reach values of about $20\delta_1$ and $2-3\delta_1$ for the longitudinal and transverse (not shown for brevity) scales, respectively. The power law decay is similar to that of the zpg cases, as can be seen for L_1 for which both ω^{-1} and $\omega^{-1.5}$ are plotted. When normalized by the internal length scale, the longitudinal coherence scale reaches $65\nu/u_\tau$ for apg19, around $1.4\times 10^2\nu/u_\tau$ for apg38, and $2.0\times 10^2\nu/u_\tau$ for apg57, and the transverse one $17\nu/u_\tau$, $22\nu/u_\tau$, and $36\nu/u_\tau$, respectively. While the low-frequency scales do not exhibit clear variation from the zpg to the apg, the high-frequency ones are indeed smaller in the apg case. For fpg, the decay rate, seen in Fig. 13, is closer to ω^{-1} than in the previously discussed cases. The upper bounds for fpg32 are $15\delta_1$ for the longitudinal scale and $2\delta_1$ for the transverse one. The corresponding high-frequency values are $1.4\times 10^2\nu/u_\tau$ and $30\nu/u_\tau$, respectively.

The ratio L_2/L_1 for apg cases is shown in Fig. 14a and exhibits trends and values similar to the one measured for zpg cases. Figure 14b shows the ratio of length scales for the fpg case. This ratio is consistently lower than for the other cases, and it is close to constant over almost a frequency decade. The strengthening of the anisotropy with comparison to apg or zpg cases supports earlier discussions on the stretching of vortices. Piomelli et al. [49], among others, studied the turbulence in fpg boundary layers and reported stretching and straightening of both streaks and coherent vortices, with an increased effect for stronger pressure gradients. These effects could be contributing factors to both the reduction of L_2 with less meandering of coherent structures and the increase of L_1.

VI. Wavenumber–Frequency Spectra

The wavenumber–frequency spectrum Φ_{pp} is obtained by taking the space-time Fourier transform of the correlation function R_{pp}:

$$\Phi_{\mathrm{pp}}(\boldsymbol{k},\omega)\equiv\frac{1}{(2\pi)^3}\int_{\mathcal{S}_m}\int_{-\infty}^{+\infty}R_{\mathrm{pp}}(\boldsymbol{r},\tau)e^{-i(\boldsymbol{k}\cdot\boldsymbol{r}-\omega\tau)}\,\mathrm{d}\tau\,\mathrm{d}\boldsymbol{r} \tag{6}$$

In practice, Φ_{pp} is computed by Fourier transforming, in space, the cross-spectra $S_{\mathrm{pp}}(\boldsymbol{r},\omega)$ that are estimated with a periodogram method. More specifically, for a given angular position of the rotating antenna, each pair of microphones associated to a unique value of separation vector is used to compute the cross-spectra. The antenna is then rotated to cover a full disk. Space Fourier transform is applied to the cross-spectra using all separation vectors in the disk. A window is applied on the amplitude of separation, to limit oscillations in the spectra. The geometry of the antenna introduces a bias in the measurement, and the measured spectra are in fact a convolution product of the true spectra with the transfer function of the antenna. Deconvolution methods can be applied to recover this true spectra. More details on both the signal processing and the deconvolution method can be found in Prigent et al. [30].

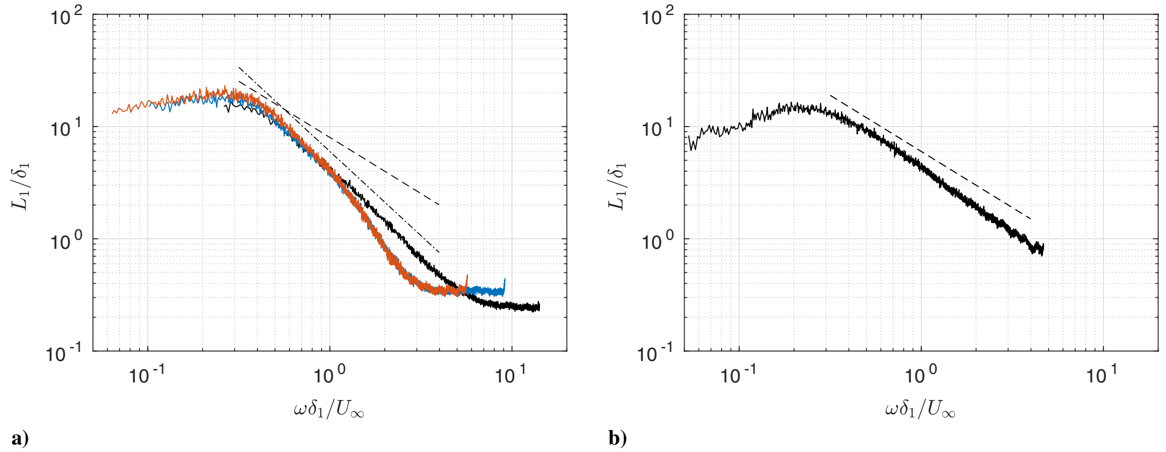

Fig. 13 Longitudinal length scales, for a) apg19 (black), apg38 (blue), and apg57 (red), and b) fpg32 cases. −1 (dashed) and −1.5 (dash-dotted) power laws for reference.

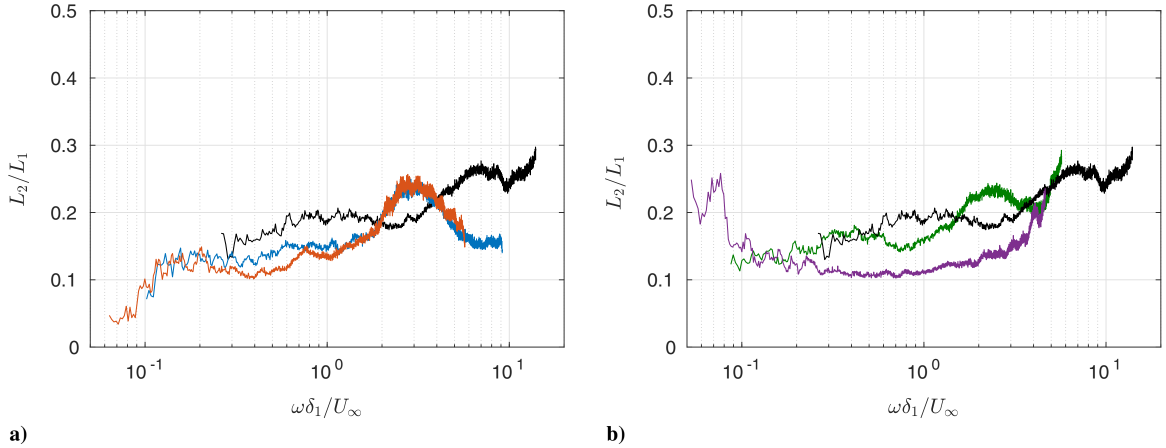

Fig. 14 Transverse-to-longitudinal length scales ratio: a) apg19 (black), apg38 (blue), and apg57 (red), and b) comparison between apg19 (black), zpg25 (green), and fpg32 (purple).

A. One-Dimensional Wavenumber–Frequency Spectra

Most of the data available in the literature is one-dimensional because it has been sampled by a linear array of microphones. Since

$$S_{\mathrm{pp}}(\boldsymbol{r},\omega) = \iint_{-\infty}^{\infty} \Phi_{\mathrm{pp}}(\boldsymbol{k},\omega)e^{+i\boldsymbol{k}.\boldsymbol{r}}\,\mathrm{d}\boldsymbol{k}$$

one has

$$S_{\mathrm{pp}}(r_1, r_2 = 0,\omega) = \int_{-\infty}^{\infty}\left(\int_{-\infty}^{\infty}\Phi_{\mathrm{pp}}(k_1,k_2,\omega)\,\mathrm{d}k_2\right)e^{+ik_1.r_1}\,\mathrm{d}k_1$$

and therefore

$$\int_{-\infty}^{\infty}\Phi_{\mathrm{pp}}(k_1,k_2,\omega)\,\mathrm{d}k_2 = \frac{1}{2\pi}\int_{-\infty}^{\infty}S_{\mathrm{pp}}(r_1,r_2=0,\omega)e^{-ik_1.r_1}\,\mathrm{d}r_1$$

Thus, the Fourier transform of the cross-spectra along r_1 only is formally equivalent to the integral of Φ_{pp} over k_2. The one-dimensional wavenumber–frequency spectra is herein written as

$$\Phi_{\mathrm{pp}}(k_1,\omega) = \int_{-\infty}^{\infty}\Phi_{\mathrm{pp}}(k_1,k_2,\omega)\,\mathrm{d}k_2 \tag{7}$$

The one-dimensional form of the classical models by Corcos [6] and Chase [5] can be expressed as follows. For the Corcos model,

$$\Phi_{\mathrm{pp}}^{\mathrm{Cor\,cos}}(k_1,\omega) = \int_{-\infty}^{\infty}\frac{S_{\mathrm{pp}}(\omega)}{\pi^2}\frac{\alpha_1 k_c}{k_c^2+\alpha_1^2(k_1-k_c)^2}\frac{\alpha_2 k_c}{k_c^2+\alpha_2^2 k_2^2}\,\mathrm{d}k_2 = \frac{S_{\mathrm{pp}}(\omega)}{\pi}\frac{\alpha_1 k_c}{k_c^2+\alpha_1^2(k_1-k_c)^2}$$

The Chase model can be recast as

$$\Phi_{\mathrm{pp}}^{\mathrm{Chase}}(\boldsymbol{k},\omega) = \rho^2 u_\tau^3\left(\frac{C_M k_1^2}{[K_+^2+(b_M\delta)^{-2}]^{5/2}} + \frac{C_T|k|^2}{[K_+^2+(b_T\delta)^{-2}]^{5/2}}\right)$$

with

$$K_+^2 = \frac{(\omega-U_c k_1)^2}{h^2 u_\tau^2} + |\boldsymbol{k}|^2$$

associated with the following numerical values of the constants $C_M = 0.0745$, $C_T = 0.0475$, $b_M = 0.756$, $b_T = 0.378$, and $h = 3$. The one-dimensional form of this spectrum is thus

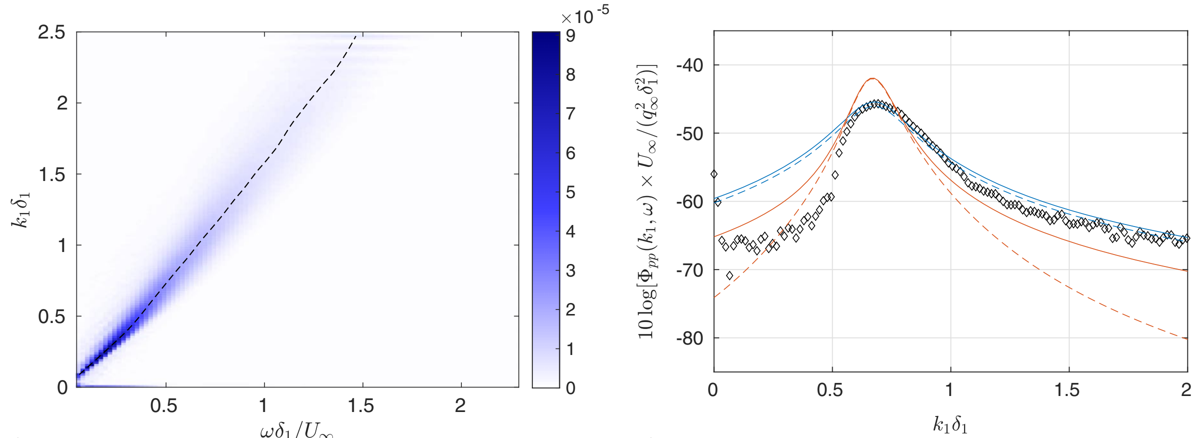

Fig. 15 Measured $\Phi_{pp}(k_1,\omega)\times U_\infty/(q_\infty^2\delta_1^2)$ for zpg45: a) $k_1-\omega$ map with the maximum of the convective ridge (dashed), and b) comparison between experimental data and Corcos ($\alpha_1 = 5, \alpha_2 = 1.2$) (blue) and Chase (red) models at $\omega\delta/u_\tau = 98$: models estimated over a k-grid of finite size and integrated over k_2 (dashed) and analytic expression (solid).

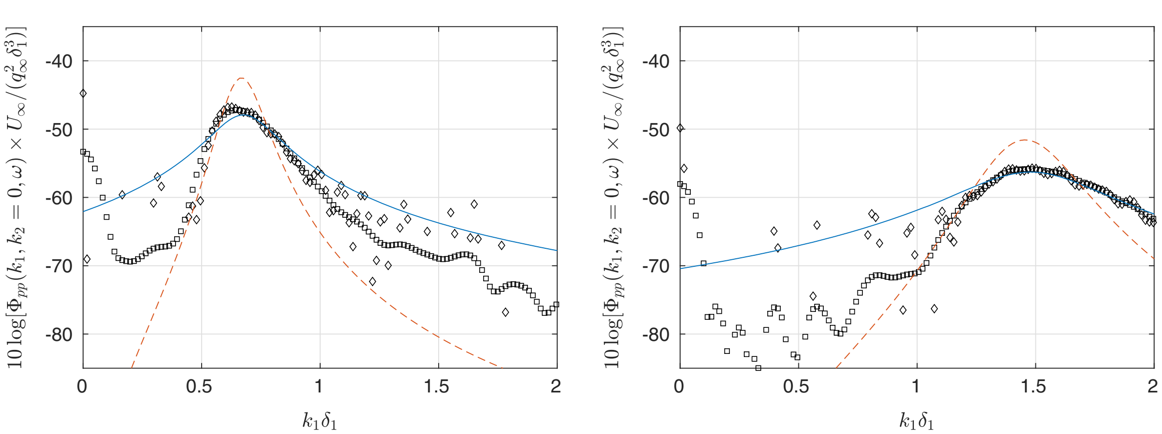

Fig. 16 Measured $\Phi_{\mathrm{pp}}(k_1,k_2=0,\omega)\times U_\infty/(q_\infty^2\delta_1^3)$ for zpg45 at a) $\omega\delta/u_\tau = 98$ and b) $\omega\delta/u_\tau = 201$. With (⋄) and without (□) deconvolution, comparison with Chase (dashed) and Corcos (plain) models, with $\alpha_1 = 5$ and $\alpha_2 = 1.2$ for the latter.

$$\Phi_{pp}^{\mathrm{Chase}}(k_1,\omega)=\rho^2u_\tau^3\times\left(\frac{4C_Mk_1^2}{3\left(\frac{(\omega-U_ck_1)^2}{h^2u_\tau^2}+(b_M\delta)^{-2}+k_1^2\right)^2}+\frac{2C_T\left(\frac{(\omega-U_ck_1)^2}{h^2u_\tau^2}+(b_T\delta)^{-2}+k_1^2\right)}{3\left(\frac{(\omega-U_ck_1)^2}{h^2u_\tau^2}+(b_T\delta)^{-2}+k_1^2\right)^2}\right)$$

The one-dimensional wavenumber–frequency spectrum for the zpg45 case is shown in Fig. 15a. The convective ridge is clearly visible; its maximum is highlighted and serves to compute the convective velocity discussed in Sec. IV. This spectrum is plotted in Fig. 15b at a fixed frequency, along with the corresponding Corcos and Chase models. As defined in Eq. (7), this spectrum is obtained by integrating over the second dimension of the wavenumber space. The computation of the full wavenumber frequency spectra is done with a specific grid of $\boldsymbol{k}$ vectors. The size of this grid can therefore influence the level of the integrated spectra. This effect is shown in Fig. 15b, for the models, by the difference between the analytic expression of the one-dimensional spectra and their two-dimensional form integrated

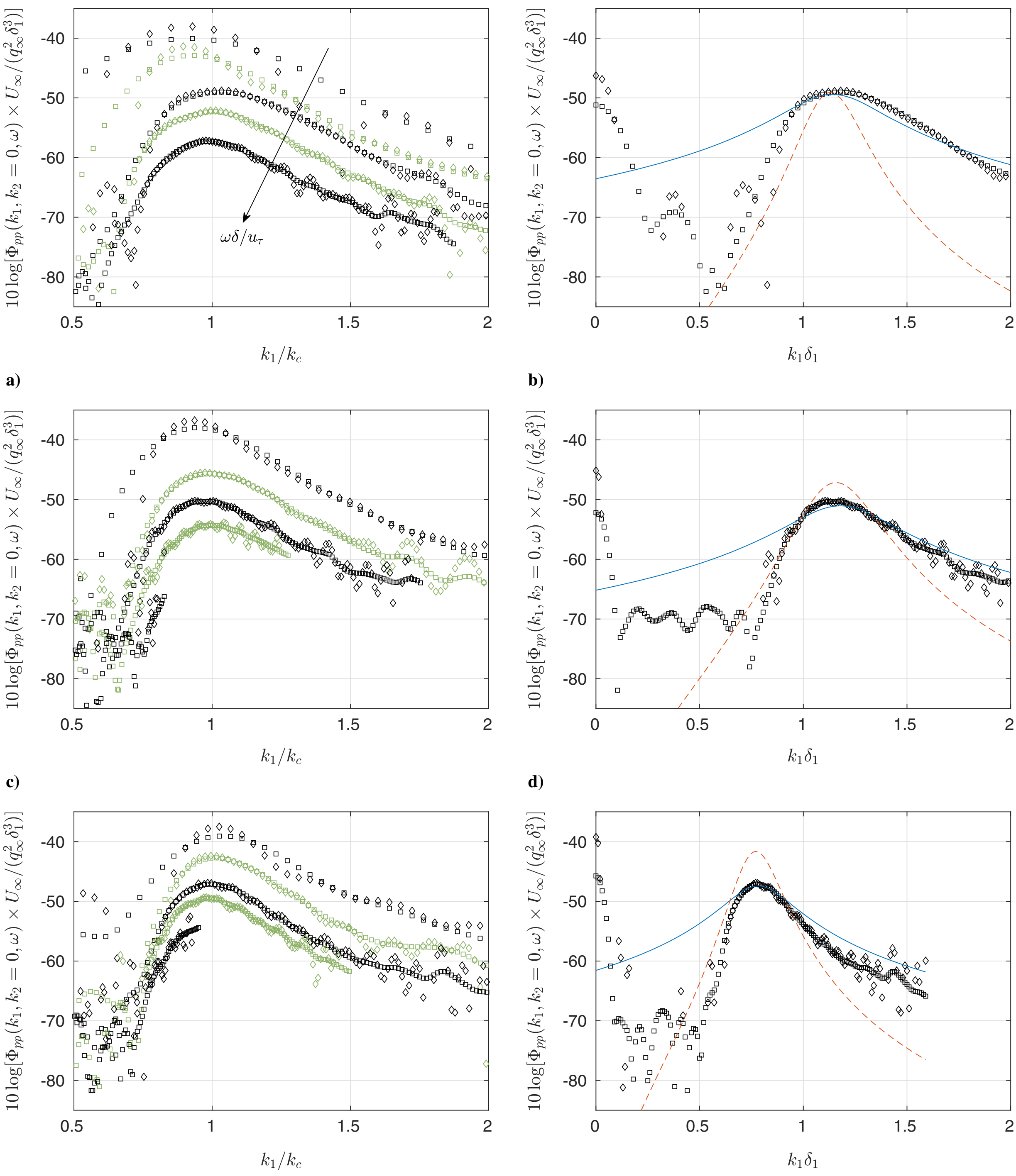

Fig. 17 **Measured $\Phi_{pp}(k_1,k_2=0,\omega)\times U_\infty/(q_\infty^2\delta_1^3)$, for apg19 (a, b), zpg25 (c, d), and fpg32 (e, f), with ($\diamond$) and without ($\square$) deconvolution. Left: $\omega\delta/u_\tau\sim 50,100,150,200,300$; right: $\omega\delta/u_\tau\sim 150$. Comparison with Chase (dashed) and Corcos (plain) models.**

over a grid of finite size. The decay rate of the model is naturally the key factor in the dependence on grid size. While the Corcos model has an exponential decay and is merely affected, the Chase model is polynomial and exhibits strong discrepancies. One of the prime interest of displaying this data is the study of spectral level in the sub- and superconvective regions, which requires an accurate comparison between models and experimental data. This approach is thus not satisfactory.

B. Two-Dimensional Wavenumber–Frequency Spectra

To avoid the previously mentioned numerical difficulty, one can directly look at section views of two-dimensional spectra by simply taking their values at $k_2 = 0$.

The wavenumber–frequency spectra for zpg45 at $k_2 = 0$ are plotted in Fig. 16 at two frequencies along with the Corcos and Chase models for comparison. Spectra are given with and without deconvolution. While it can correct the spectrum level, in particular for the convective ridge and better the rendering of acoustic components, it can also introduce some oscillations. Out of fairness for the comparison, both datasets are thus shown simultaneously. The asymmetry of the convective ridge is clearly visible, where the spectra decay faster toward the lower wavenumber than toward the higher ones. Despite correctly matching the convective ridge maxima, Corcos model rapidly fails to predict the decay, in particular in the subconvective region where the experimental data decays much faster, before this decay slows down and the level remains around a decade lower than the model. On the other hand, Chase model appears to satisfactorily predict the decay rate for wavenumbers lower than but close to the convective one. However, this latter model fails to match criteria that are the high wavenumber decay rate, the level of the ridge itself, and the slower decay rate in the subconvective region.

The spectra at $k_2 = 0$ at lower velocities and for the three pressure gradient cases are plotted in Fig. 17. Deconvolution appears particularly interesting for the low frequencies, for which the convective ridge is the narrowest, before the k_1/k_c normalization, and hence the most affected by the width of the antenna's transfer function. Overall, the different cases exhibit similar trends, with a rapid decay of the ridge toward the low wavenumbers and a slower decay toward the high ones. Relatively to its convective wavenumber, the apg cases have wider convective ridges. Comparison with Chase and Corcos models shows that both fail to describe the behavior of the spectra, for the three cases. While the rapid decay of the Chase model is certainly interesting on the low wavenumber edge of the convective ridge, it fails to predict both the slower decay when reaching even lower wavenumbers and the maximum of the ridge. Corcos model better predicts the ridge maximum and its high wavenumber edge, even more so in the fpg case, but fails in the subconvective range with an overestimation of about 10 dB.

Cohen and Gloerfelt [16] showed spectra obtained from numerical simulations with five values of the pressure gradient, with both adverse and favorable cases, normalized using alternatively δ and δ_1 for comparison. They found that δ offered the best collapse of the convective ridge, regarding its level and the position of its maximum on the $k_1\delta$ axis. On the contrary, the values were found to slightly differ with δ_1. Working with experimental data, however, its determination is more reliable than that of δ itself, hence the choice of the current normalization. The authors found the ridge to be wider in apg cases than in both zpg and fpg ones, whatever the normalization used. With δ_1, fpg data showed a slightly narrower ridge than the zpg case. This trend is also found in the present results, with a wider convective ridge for apg than the two others, in particular, fpg, which exhibits the narrowest with a difference more striking than in Cohen and Gloerfelt [16].

Figure 18 shows the two-dimensional wavenumber–frequency spectra $\Phi_{pp}(k_1, k_2, \omega)$ at $\omega\delta/u_\tau \sim 150$ for the three pressure gradients at inlet velocity $U_0 = 25\ \mathrm{m \cdot s^{-1}}$. While the asymmetry of the convective ridge is not as obvious as in the $k_2 = 0$ plots, one notices the characteristic elongated shape. The aspect ratio is smaller for the apg case than for zpg and even more so than for the fpg. The latter is indeed relatively more elongated along k_2. Once more, these observations support the numerical findings from [16] about the smaller aspect ratio for apg.

The modification of the aspect ratio of the convective ridge could be explained by the discussion on the straightening and stretching of coherent structures and the observed variation of the ratio of coherence length scales. Although there is no direct observation of such mechanism in the flows currently studied, these repeated observations are well in line with this possibility.

VII. Conclusions

Measurements have been conducted in turbulent boundary layers subjected to various pressure gradients. Velocity profiles collapse onto existing experimental data, and the well-known effects of pressure gradients are found with an increase of both mean velocity and turbulence intensity in the outer region, going from favourable to adverse pressure gradients. The main focus of the study is on spatial structure and wavenumber spectra of wall pressure fluctuations. Recent advances in measurement technology and data processing offer reliable data, and enable the computation of two-dimensional wavenumber frequency spectra.

Owing to the spatial resolution of the antenna, the coherence scales have been finely computed and their decay rate discussed. The ratio of transverse to longitudinal scales is significantly reduced for the fpg case.

For all pressure gradients, wavenumber frequency spectra exhibit the known asymmetry of the convective ridge with a faster decay toward the low wavenumbers than toward the high ones. Corcos model satisfactorily matches the maximum of the convective ridge and offers a fair estimate of the initial decay toward the high wavenumber. However, it fails at rendering the low wavenumber or subconvective range of the spectra. The Chase model, while being closer to the decay rate found in the low-wavenumber part of the ridge, fails

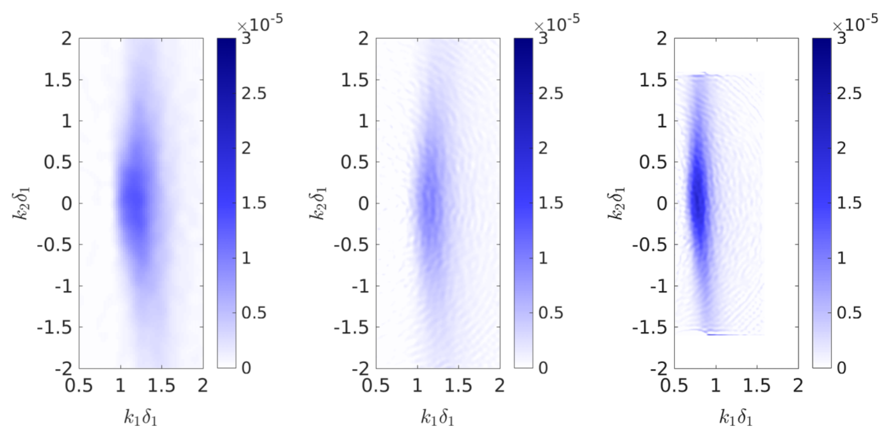

Fig. 18 $\Phi_{pp}(k_1,k_2,\omega) \times U_\infty/(q_\infty^2\delta_1^3)$ **after deconvolution at** $\omega\delta/u_\tau \sim 150$ **for apg19 (a), zpg25 (b), and fpg32 (c).**

to render the correct levels. While no clear plateau is found in the subconvective range, there is a change in the decay rate that leads to a much slower one. The aspect ratio of the two-dimensional wavenumber frequency spectrum's convective ridge increases from adverse to zero- and favourable pressure gradients.

In the current results, apg flows lead to a significantly higher convection velocity, by up to 14%, compared to the zpg flows. This result differs from what had been reported in the literature, where despite the scatter of reported values, all apg flows had been reported to reduce the convection velocity to some extent.

Mechanisms have been discussed that could account for those results, based on previous findings on velocity structures and vortices within the boundary layer. Favorable pressure gradients were reported to straighten and stretch near-wall structures and vortices, leading to fewer but longer and more intense vortices. As a result, the friction velocity is increased, which is seen in the present study both in measurement of u_τ and in the levels of the normalized spectra. Furthermore, both the straightening and stretching effects should lead to a reduction of the ratio of transverse to longitudinal coherence scales. Adverse pressure gradients were reported to increase the large scale content of the turbulent boundary layers. Given that these scales are associated with higher convective velocity, the wall pressure fluctuations' convective velocity should in turn increase from zpg flows to apg ones. This explanation for apg is compelling, but a physical mechanism that could explain the effect of fpg, and perhaps the variations between studies, is still to be found.

Appendix A: Microphone Calibration Procedure

A. 1. Pin-Hole Calibration

The calibration of the pinhole microphone is divided into a low-frequency and a high-frequency parts. The low-frequency calibration itself is done in two steps. First, the pinhole microphone is compared to a reference microphone. More precisely, a calibration tube is placed above the pinhole microphone and the reference microphone is mounted near its open end, as sketched in Fig. A1. A loudspeaker is then used to generate a white noise over a wide range of frequencies, from 10 Hz to 15 kHz, which propagates through the tube. The transfer function between the pinhole and the reference microphone, written $F_1 = H_p/H_{\mathrm{ref}}$, is thus measured. Secondly, the same setup is placed above a flush-mounted 1/8-inch Bruel and Kjaer microphone type 4138 (see Fig. A2), and the new transfer function $F_2 = H_{fl}/H_{\mathrm{ref}}$ is measured. Under the assumption that the flush-mounted microphone response is flat in this frequency range, that is, $H_{fl} \equiv 1$, one obtains the frequency response of the pinhole microphone by dividing the two measured transfer functions: $H_p = F_1/F_2$. Such method is valid up to the cutoff frequency of the calibration tube, around 17 kHz.

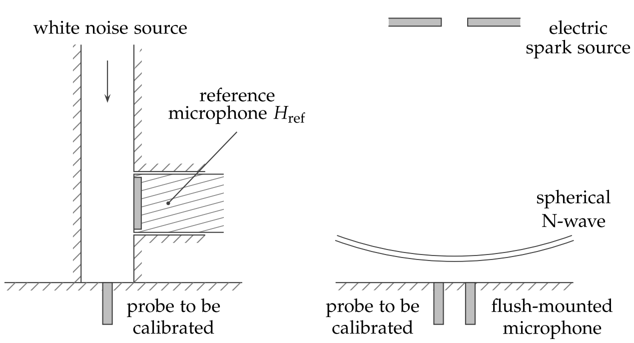

Fig. A1 Left: sketch of the calibration tube used up to the cutoff frequency of the tube. Right: high-frequency calibration using a spark source.

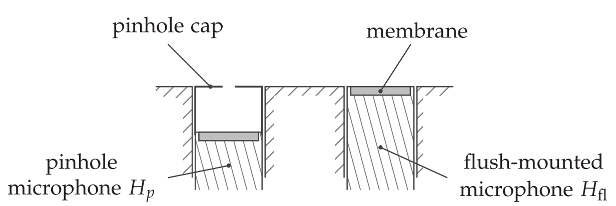

Fig. A2 Sketch of the pinhole microphone and of the flush-mounted microphone used for the calibration.

The high-frequency part of the calibration covers the range of frequencies that lie above the calibration tube's cutoff. To reach high frequencies, up to 30 kHz, a short-duration and high-pressure shock wave is generated by an electric spark source [60,61]. The spark source is made of two tungsten electrodes, separated by a gap of 20 mm, connected to a high voltage supply. Both pinhole and flush-mounted microphones are then placed at an equal distance from the spark source, as depicted in Fig. A1. The frequency response of the pinhole microphone is obtained by assuming again that the flush-mounted one has a flat response. Finally, the two calibration curves are combined to derive the whole transfer function H_p of the pinhole microphone.

Although the calibration has been conducted without flow, the hump associated with the cavity beneath the pinhole cap depends on the mean velocity. The final calibration curve has been parameterized with a second-order low-pass filter [62] to correct for this:

$$H(f) = \frac{S_0}{1 + (i/q)(f/f_r) - (f/f_r)^2}$$

where $i^2 = -1$, $q = q(U_\infty)$ is the quality factor set so that there be no discontinuity in the spectra slope, $f_r = f_r(U_\infty)$ is the resonance frequency, and S_0 is a constant.

A. 2. Remote Microphone Calibration

The remote microphones have a cutoff frequency lower than that of the calibration tube. Therefore, only a low-frequency calibration is performed to get the transfer function H of each remote probe, following the previously discussed method.

A. 3. Transducer Resolution Correction

The geometrical characteristics of the chosen pin-hole impose a sensing area that dampens the high-frequency part of the measured spectra, because of spatial integration of the fluctuations. Such averaging attenuates the spectra for frequencies as low as $\omega^+ \simeq 1$ for $d_p^+ \geq 19$ [41,43]. A correction has therefore been applied, following the methodology presented by [40], using the dimensionless frequency $S_p = \omega d_p/(2U_c)$, with $U_c = 0.6 \times U_\infty$. With the present data, the dimensionless pinhole diameter falls in the interval $16 \leq d_p^+ \leq 90$ for the zero-pressure-gradient boundary layers and $S_p \leq 2.1$.

Appendix B: Antenna Geometry

B.1. Transducer Resolution Correction

As mentioned in Sec. II.F, the antenna is composed of 63 remote microphones positioned along a line placed on a rotating disk. The distribution of the microphones is shown in Fig. B1. A nonuniform placement is used to maximize the number of unique separation vectors, and the symmetry with respect to the origin is preserved to reduce the measurement time by allowing a half rotation of the disk.

Fourier transformation in space is carried out by using all possible separation vectors and assuming homogeneity of the pressure field.

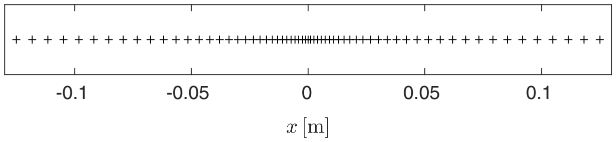

Fig. B1 Microphone positions on the rotating line.

These vectors form the so-called co-array of the antenna, with a minimum separation of 1 mm. Each angular position leads to 856 positive separation values. This density enables a satisfactory computation of the wave-number frequency spectra, although some distortion remains that are due to the transfer function of the antenna. Details of the computation method and of the deconvolution can be found in [30].

Acknowledgments

The experimental measurements were conducted within the project SONOBL (ANR-2011-BS09-035-02), funded by the French National Research Agency (ANR). The present data analysis has been conducted as part of the project BRIO, funded by the Auvergne-Rhône-Alpes region (AURA—909 92 204181). This work was performed within the framework of the Labex CeLyA of the Université de Lyon, within the program "Investissements d′Avenir" (ANR-10-LABX-0060/ANR-16-IDEX-0005) operated by the French National Research Agency.

References

[1] Graham, W. R., "A Comparison of Models for the Wavenumber-Frequency Spectrum of Turbulent Boundary Layer Pressures," *Journal of Sound and Vibration*, Vol. 206, No. 4, 1997, pp. 430–454.
https://doi.org/10.1006/jsvi.1997.1114

[2] Wilby, J. F., "Aircraft Interior Noise," *Journal of Sound and Vibration*, Vol. 190, No. 3, 1996, pp. 545–564.
https://doi.org/10.1006/jsvi.1996.0078

[3] Blake, W. K., "Essentials of Turbulent Wall-Pressure Fluctuations," *Mechanics of Flow-Induced Sound and Vibration, Vol. II Complex Flow-Structure Interactions*, Academic Press, Orlando, FL, 1986.

[4] Sevik, M. M., "Topics in Hydro-Acoustics," *Aero- and Hydro-Acoustics*, Springer–Verlag, Berlin, 1986, pp. 285–308.

[5] Chase, D. M., "Modeling the Wavevector-Frequency Spectrum of Turbulent Boundary Layer Wall Pressure," *Journal of Sound and Vibration*, Vol. 70, No. 1, 1980, pp. 29–67.
https://doi.org/10.1016/0022-460X(80)90553-2

[6] Corcos, G. M., "The Structure of the Turbulent Pressure Field in Boundary-Layer Flows," *Journal of Fluid Mechanics*, Vol. 18, No. 3, 1964, pp. 353–378.
https://doi.org/10.1017/S002211206400026X

[7] Farabee, T. M., and Casarella, M. J., "Spectral Features of Wall Pressure Fluctuations Beneath Turbulent Boundary Layer," *Physics of Fluids A*, Vol. 3, No. 10, 1991, pp. 2410–2420.
https://doi.org/10.1063/1.858179

[8] Schloemer, H. H., "Effects of Pressure Gradient on Turbulent-Boundary-Layer Wall-Pressure Fluctuations," *Journal of the Acoustical Society of America*, Vol. 42, No. 1, 1967, pp. 93–113.
https://doi.org/10.1121/1.1910581

[9] Na, Y., and Moin, P., "The Structure of Wall-Pressure Fluctuations in Turbulent Boundary Layers with Adverse Pressure Gradient and Separation," *Journal of Fluid Mechanics*, Vol. 337, 1998, pp. 347–373.
https://doi.org/10.1017/S0022112098003218

[10] Bull, M. K., "Wall-Pressure Fluctuations Beneath Turbulent Boundary Layers: Some Reflections on Forty Years of Research," *Journal of Sound and Vibration*, Vol. 190, No. 3, 1996, pp. 299–315.
https://doi.org/10.1006/jsvi.1996.0066

[11] Willmarth, W. W., "Pressure Fluctuations Beneath Turbulent Boundary Layers," *Annual Review of Fluid Mechanics*, Vol. 7, No. 1, 1975, pp. 13–36.
https://doi.org/10.1146/annurev.fl.07.010175.000305

[12] Goody, M., "Empirical Spectral Model of Surface Pressure Fluctuations," *AIAA Journal*, Vol. 42, No. 9, 2004, pp. 1788–1794.
https://doi.org/10.2514/1.9433

[13] Lee, S., "Empirical Wall-Pressure Spectral Modeling for Zero and Adverse Pressure Gradient Flows," *AIAA Journal*, Vol. 56, No. 5, 2018, pp. 1818–1829.
https://doi.org/10.2514/1.J056528

[14] Prigent, S. L., Salze, E., Jondeau, E., and Bailly, C., "Spatial Structure and Wavenumber Filtering of Wall Pressure Fluctuations on a Full-Scale Cockpit Model," *Experiments in Fluids*, Vol. 61, No. 9, 2020, pp. 1–14.
https://doi.org/10.1007/s00348-020-03017-2

[15] Hu, N., and Herr, M., "Characteristics of Wall Pressure Fluctuations for a Flat Plate Turbulent Boundary Layer with Pressure Gradients," *22nd AIAA/CEAS Aeroacoustics Conference*, AIAA Paper 2016-2749, 2016.
https://doi.org/10.2514/6.2016-2749

[16] Cohen, E., and Gloerfelt, X., "Influence of Pressure Gradients on Wall Pressure Beneath a Turbulent Boundary Layer," *Journal of Fluid Mechanics*, Vol. 838, 2018, pp. 715–758.
https://doi.org/10.1017/jfm.2017.898

[17] Smol'yakov, A. V., "A New Model for the Cross Spectrum and Wavenumber-Frequency Spectrum of Turbulent Pressure Fluctuations in a Boundary Layer," *Acoustical Physics*, Vol. 52, No. 3, 2006, pp. 331–337.
https://doi.org/10.1134/S1063771006030146

[18] Salze, E., Bailly, C., Marsden, O., Jondeau, E., and Juvé, D., "An Experimental Characterization of Wall Pressure Wavenumber-Frequency Spectra in the Presence of Pressure Gradients," *20th AIAA/CEAS Aeroacoustics Conference*, AIAA Paper 2014-2909, 2014.
https://doi.org/10.2514/6.2014-2909

[19] Catlett, M. R., Anderson, J. M., Forest, J. B., and Stewart, D. O., "Empirical Modeling of Pressure Spectra in Adverse Pressure Gradient Turbulent Boundary Layers," *AIAA Journal*, Vol. 54, No. 2, 2016, pp. 569–587.
https://doi.org/10.2514/1.J054375

[20] Fritsch, D., Vishwanathan, V., Lowe, K. T., and Devenport, W. J., "The Space-Time Correlation of Pressure Under High Reynolds Number Smooth Wall Turbulent Boundary Layers in Pressure Gradient Family," *AIAA Scitech 2021 Forum*, AIAA Paper 2021-1946, 2021.
https://doi.org/10.2514/6.2021-1946

[21] Burton, T. E., "Wall Pressure Fluctuations at Smooth and Rough Surfaces Under Turbulent Boundary Layers with Favorable and Adverse Pressure Gradients," Acoustics and Vibration Lab. TR AD 772 548, Massachusetts Inst. of Technology, 1973.

[22] Juvé, D., Prigent, S. L., Salze, E., Souchotte, P., and Bailly, C., "Opening Lectures—Wall-Pressure Wavenumber-Frequency Spectra: Experimental Challenges and Recent Advances," *Flinovia— Flow Induced Noise and Vibration Issues and Aspects-III. FLINOVIA 2019*, edited by Ciappi, E., et al., Springer, Cham, 2021.
https://doi.org/10.1007/978-3-030-64807-7_1

[23] Abraham, B. M., and Keith, W. L., "Direct Measurements of Turbulent Boundary Layer Wall Pressure Wavenumber-Frequency Spectra," *Journal of Fluids Engineering*, Vol. 120, No. 1, 1998, pp. 29–39.
https://doi.org/10.1115/1.2819657

[24] Blake, W. K., and Chase, D. M., "Wavenumber-Frequency Spectra of Turbulent-Boundary-Layer Pressure Measured by Microphone Arrays," *Journal of the Acoustical Society of America*, Vol. 49, No. 3B, 1971, pp. 862–877.
https://doi.org/10.1121/1.1912427

[25] Panton, R. L., and Robert, G., "The Wavenumber-Phase Velocity Representation for the Turbulent Wall-Pressure Spectrum," *Journal of Fluid Engineering*, Vol. 480, 1994, No. 116, pp. 477–483.
https://doi.org/10.1115/1.2910301

[26] Arguillat, B., Ricot, D., Bailly, C., and Robert, G., "Measured Wavenumber: Frequency Spectrum Associated with Acoustic and Aerodynamic Wall Pressure Fluctuations," *Journal of the Acoustical Society of America*, Vol. 128, No. 4, 2010, pp. 1647–1655.
https://doi.org/10.1121/1.3478780

[27] Haxter, S., and Spehr, C., "Up in the Air: In-Flight Wavenumber Characterization of Surface Pressure Fluctuations at Transonic Conditions," *2018 AIAA/CEAS Aeroacoustics Conference*, AIAA Paper 2018-3275, 2018.
https://doi.org/10.2514/6.2018-3275

[28] Maxit, L., "Simulation of the Pressure Field Beneath a Turbulent Boundary Layer Using Realizations of Uncorrelated Wall Plane Waves," *Journal of the Acoustical Society of America*, Vol. 140, No. 2, 2016, pp. 1268–1285.
https://doi.org/10.1121/1.4960516

[29] Robin, O., Moreau, S., Padois, T., and Berry, A., "Measurement of the Wavenumber-Frequency Spectrum of Wall Pressure Fluctuations: Spiral-Shaped Rotative Arrays with Pinhole-Mounted Quarter Inch Microphones," *19th AIAA/CEAS Aeroacoustics Conference*, AIAA Paper 2013-2058, 2013.
https://doi.org/10.2514/6.2013-2058

[30] Prigent, S. L., Salze, E., and Bailly, C., "Deconvolution of the Wavenumber-Frequency Spectra of Wall Pressure Fluctuations," *AIAA Journal*, Vol. 58, No. 1, 2020, pp. 164–173.
https://doi.org/10.2514/1.J058203

[31] Dixit, S. A., and Ramesh, O. N., "Pressure-Gradient-Dependent Logarithmic Laws in Sink Flow Turbulent Boundary Layers," *Journal of Fluid Mechanics*, Vol. 615, 2008, pp. 445–475.
https://doi.org/10.1017/S0022112008004047

[32] Elsinga, G. E., and Marusic, I., "Evolution and Lifetimes of Flow Topology in a Turbulent Boundary Layer," *Physics of Fluids*, Vol. 22,

No. 1, 2010, Paper 015102.
https://doi.org/10.1063/1.3291070
[33] Clauser, F. H., "Turbulent Boundary Layers in Adverse Pressure Gradients," *Journal of the Aeronautical Sciences*, Vol. 21, No. 2, 1954, pp. 91–108.
https://doi.org/10.2514/8.2938
[34] Esteban, L. B., Dogan, E., Rodríguez-López, E., and Ganapathisubramani, B., "Skin-Friction Measurements in a Turbulent Boundary Layer Under the Influence of Free-Stream Turbulence," *Experiments in Fluids*, Vol. 58, No. 9, 2017, p. 115.
https://doi.org/10.1007/s00348-017-2397-8
[35] Rodríguez-López, E., Bruce, P. J., and Buxton, O. R., "A Robust Post-Processing Method to Determine Skin Friction in Turbulent Boundary Layers from the Velocity Profile," *Experiments in Fluids*, Vol. 56, No. 4, 2015, p. 68.
https://doi.org/10.1007/s00348-015-1935-5
[36] Harun, Z., Monty, J. P., Mathis, R., and Marusic, I., "Pressure Gradient Effects on the Large-Scale Structure of Turbulent Boundary Layers," *Journal of Fluid Mechanics*, Vol. 715, 2013, pp. 477–498.
https://doi.org/10.1017/jfm.2012.531
[37] Hutchins, N., Nickels, T. B., Marusic, I., and Chong, M. S., "Hot-Wire Spatial Resolution Issues in Wall-Bounded Turbulence," *Journal of Fluid Mechanics*, Vol. 635, 2009, pp. 103–136.
https://doi.org/10.1017/S0022112009007721
[38] Österlund, J. M., "Experimental Studies of Zero Pressure-Gradient Turbulent Boundary Layer Flow," Doctoral Dissertation, Royal Inst. of Technology (KTH), Stockholm, 1999.
[39] Chauhan, K. A., Monkewitz, P. A., and Nagib, H. M., "Criteria for Assessing Experiments in Zero Pressure Gradient Boundary Layers," *Fluid Dynamics Research*, Vol. 41, No. 2, 2009, Paper 021404.
https://doi.org/10.1088/0169-5983/41/2/021404
[40] Corcos, G. M., "Resolution of Pressure in Turbulence," *Journal of the Acoustical Society of America*, Vol. 35, No. 2, 1963, pp. 192–199.
https://doi.org/10.1121/1.1918431
[41] Schewe, G., "On the Structure and Resolution of Wall-Pressure Fluctuations Associated with Turbulent Boundary-Layer Flow," *Journal of Fluid Mechanics*, Vol. 134, 1983, pp. 311–328.
https://doi.org/10.1017/S0022112083003389
[42] Olivero-Bally, P., Forestier, B. E., Focquenoy, E., and Olivero, P., "Wall-Pressure Fluctuations in Natural and Manipulated Turbulent Boundary Layers in Air and Water," *ASME-PUBLICATIONS-FED*, Vol. 168, 1993, pp. 63–74.
[43] Gravante, S. P., Naguib, A. M., Wark, C. E., and Nagib, H. M., "Characterization of the Pressure Fluctuations Under a Fully Developed Turbulent Boundary Layer," *AIAA Journal*, Vol. 36, No. 10, 1998, pp. 1808–1816.
https://doi.org/10.2514/2.296
[44] Bull, M. K., and Thomas, A. S. W., "High Frequency Wall-Pressure Fluctuations in Turbulent Boundary Layers," *Physics of Fluids*, Vol. 19, No. 4, 1976, pp. 597–599.
https://doi.org/10.1063/1.861496
[45] Goody, M. C., and Simpson, R. L., "Surface Pressure Fluctuations Beneath Two- and Three-Dimensional Turbulent Boundary Layers," *AIAA Journal*, Vol. 38, No. 10, 2000, pp. 1822–1831.
https://doi.org/10.2514/2.863
[46] Blake, W. K., "Turbulent Boundary-Layer Wall-Pressure Fluctuations on Smooth and Rough Walls," *Journal of Fluid Mechanics*, Vol. 44, No. 4, 1970, pp. 637–660.
https://doi.org/10.1017/S0022112070002069
[47] Meyers, T., Forest, J. B., and Devenport, W. J., "The Wall-Pressure Spectrum of High-Reynolds-Number Turbulent Boundary-Layer Flows over Rough Surfaces," *Journal of Fluid Mechanics*, Vol. 768, 2015, pp. 261–293.
https://doi.org/10.1017/jfm.2014.743
[48] Küchler, C., Bewley, G., and Bodenschatz, E., "Experimental Study of the Bottleneck in Fully Developed Turbulence," *Journal of Statistical Physics*, Vol. 175, No. 3, 2019, pp. 617–639.
https://doi.org/10.1007/s10955-019-02251-1
[49] Piomelli, U., Balaras, E., and Pascarelli, A., "Turbulent Structures in Accelerating Boundary Layers," *Journal of Turbulence*, Vol. 1, No. 1, 2000, pp. 1–16.
https://doi.org/10.1088/1468-5248/1/1/001
[50] Bourassa, C., and Thomas, F. O., "An Experimental Investigation of a Highly Accelerated Turbulent Boundary Layer," *Journal of Fluid Mechanics*, Vol. 634, 2009, pp. 359–404.
https://doi.org/10.1017/S0022112009007289
[51] Romano, G. P., "Analysis of Two-Point Velocity Measurements in Near-Wall Flows," *Experiments in Fluids*, Vol. 20, No. 2, 1995, pp. 68–83.
https://doi.org/10.1007/BF00189296
[52] Renard, N., and Deck, S., "On the Scale-Dependent Turbulent Convection Velocity in a Spatially Developing Flat Plate Turbulent Boundary Layer at Reynolds Number $\mathrm{Re}_\theta = 13000$," *Journal of Fluid Mechanics*, Vol. 775, 2015, pp. 105–148.
https://doi.org/10.1017/jfm.2015.290
[53] Willmarth, W. W., and Wooldridge, C. E., "Measurements of the Fluctuating Pressure at the Wall Beneath a Thick Turbulent Boundary Layer," *Journal of Fluid Mechanics*, Vol. 14, No. 2, 1962, pp. 187–210.
https://doi.org/10.1017/S0022112062001160
[54] Bull, M. K., "Wall-Pressure Fluctuations Associated with Subsonic Turbulent Boundary Layer Flow," *Journal of Fluid Mechanics*, Vol. 28, No. 4, 1967, pp. 719–754.
https://doi.org/10.1017/S0022112067002411
[55] Hutchins, N., and Marusic, I., "Evidence of Very Long Meandering Features in the Logarithmic Region of Turbulent Boundary Layers," *Journal of Fluid Mechanics*, Vol. 579, 2007, pp. 1–28.
https://doi.org/10.1017/S0022112006003946
[56] Monty, J. P., Harun, Z., and Marusic, I., "A Parametric Study of Adverse Pressure Gradient Turbulent Boundary Layers," *International Journal of Heat and Fluid Flow*, Vol. 32, 2011, pp. 575–585.
https://doi.org/10.1016/j.ijheatfluidflow.2011.03.004
[57] Chung, D., and McKeon, B., "Large-Eddy Simulation of Large-Scale Structures in Long Channel Flow," *Journal of Fluid Mechanics*, Vol. 661, 2010, pp. 341–364.
https://doi.org/10.1017/S0022112010002995
[58] Del Alamo, J. C., and Jiménez, J., "Estimation of Turbulent Convection Velocities and Corrections to Taylor's Approximation," *Journal of Fluid Mechanics*, Vol. 640, 2009, pp. 5–26.
https://doi.org/10.1017/S0022112009991029
[59] Monty, J. P., Hutchins, N., Ng, H. C. H., Marusic, I., and Chong, M. S., "A Comparison of Turbulent Pipe, Channel and Boundary Layer Flows," *Journal of Fluid Mechanics*, Vol. 632, 2009, pp. 431–442.
https://doi.org/10.1017/S0022112009007423
[60] Ollivier, S., Salze, E., Averiyanov, M., Yuldashev, P., Khokhlova, V., and Blanc-Benon, P., "Calibration Method for High Frequency Microphones," *Acoustics 2012*, 2012, pp. 3503–3507, https://www.conforg.fr/acoustics2012/cdrom/data/articles/000624.pdf.
[61] Salze, E., Ollivier, S., Blanc-Benon, P., Yuldashev, P., Averiyanov, M., and Khokhlova, V., "Characterisation of the Sound Field Emitted by an Electric Spark Source in Air," *6th Forum Acusticum*, European Acoustics Assoc., 2011, pp. 323–326.
[62] Goody, M. C., "An Experimental Investigation of Pressure Fluctuations in Three-Dimensional Turbulent Boundary Layers," Ph.D. Dissertation, Virginia Polytechnic Inst. and State Univ., Blackburg, VA, 1999.

N. D. Sandham
Associate Editor